Stripe domains reorientation in ferromagnetic films with perpendicular magnetic anisotropy

Louis-Charles Garnier, Massimiliano Marangolo, Mahmoud Eddrief, Diego Bisero, Samuele Fin, Francesca Casoli, Maria Gloria Pini, Angelo Rettori, Silvia Tacchi

Stripe domains reorientation in ferromagnetic films with perpendicular magnetic anisotropy

Louis-Charles Garnier[1,2], Massimiliano Marangolo[1], Mahmoud Eddrief[1], Diego Bisero[3,4], Samuele Fin[3], Francesca Casoli[5], Maria Gloria Pini[6], Angelo Rettori[7,8], Silvia Tacchi[9]

[1] Sorbonne Université, CNRS, Institut des NanoSciences de Paris, INSP, F-75005 Paris, France

[2] Laboratoire d'Ingénierie des Systèmes de Versailles (LISV), Université Versailles St-Quentin, Bâtiment Boucher, Pôle scientifique et technologique de Vélizy, 1-12 avenue de l'Europe, F-78140 Vélizy, France

[3] Dipartimento di Fisica e Scienze della Terra, Università degli Studi di Ferrara, Via Saragat 1, I-44122 Ferrara, Italy

[4] Consorzio Nazionale Interuniversitario per le Scienze Fisiche della Materia (CNISM), Unità di Ferrara, I-44122 Ferrara, Italy

[5] Consiglio Nazionale delle Ricerche (CNR), Istituto dei Materiali per l'Elettronica ed il Magnetismo (IMEM), Parco Area delle Scienze 37/A, 43124 Parma, Italy

[6] Consiglio Nazionale delle Ricerche (CNR), Istituto dei Sistemi Complessi (ISC), Unità di Firenze, I-50019 Sesto Fiorentino, Italy

[7] Dipartimento di Fisica ed Astronomia, Università degli Studi di Firenze, Via G. Sansone 1, I-50019 Sesto Fiorentino, Italy

[8] Consorzio Nazionale Interuniversitario per le Scienze Fisiche della Materia (CNISM), Unità di Firenze, I-50019 Sesto Fiorentino, Italy

[9] Consiglio Nazionale delle Ricerche (CNR), Istituto Officina dei Materiali (IOM), Unità di Perugia, c/o Dipartimento di Fisica e Geologia, Università degli Studi di Perugia, I-06123 Perugia, Italy

E-mail: `tacchi@iom.cnr.it`

14 October 2019

Abstract. Ferromagnetic thin films with moderate perpendicular magnetic anisotropy (PMA) are known to support weak stripe domains provided film thickness exceeds a critical value. In this work, we performed both an experimental and theoretical investigation of a peculiar phenomenon shown by weak stripe domains: namely, the stripe domains reorientation when a dc magnetic field is applied in the film plane along the direction perpendicular to the stripes axis. We focus on bct α'-Fe_8N_{1-x} thin films obtained by N_2^+ irradiation of α-Fe films epitaxially grown on ZnSe/GaAs(001). By using different ion implantation and heat treatment conditions, we show that it is possible to tune the PMA values. Magnetic force microscopy and vibrating sample magnetometer measurements prove the existence of weak stripe domains at remanence, and of a threshold field for the reorientation of the stripes axis in a transversal field. Using a one-dimensional model of the magnetic stripe domains, where the essential parameter is the maximum canting angle of the stripe magnetization out of the film plane, the various contributions to the magnetic energy can be separately calculated. A linear increase of the reorientation threshold field

on the PMA is obtained, in qualitative agreement with experimental data in our Fe-N films, as well as in other thin films with weak stripe domains. Finally, we find that also the rotatable anisotropy field linearly increases as a function of the PMA magnitude.

Submitted to: *JPhysMaterials (focus issue: Spin Dependent Phenomena in New Materials)*
Keywords: magnetic films, magnetic anisotropy, magnetic domains

1. Introduction

The formation of stripe domain patterns has been observed in a variety of physical systems [1, 2, 3, 4, 5] as a consequence of competing interactions acting on different spatial scales. In thin ferromagnetic films with a perpendicular component in the magnetic anisotropy energy, magnetic domains appear as stripes with alternating (up and down) out-of-plane orientation of the magnetization. Magnetic stripe domains occur due to the competition between different contributions to the magnetic free energy: above all, the short-range exchange coupling, the long-range magnetostatic interaction, and the perpendicular magnetic anisotropy (PMA). Magnetic stripe structures are usually classified depending on the quality factor $Q = K_{PMA}/K_d$ [6], namely on the ratio between the PMA energy density, K_{PMA}, and the magnetostatic energy density, $K_d = 2\pi M_s^2$, where M_s is the saturation magnetization of the system.

In systems with high PMA compared to the magnetostatic energy, i.e., with $Q \gg 1$, stripe/band domains occur even for extremely low thickness. This kind of stripe domains is characterised by thin domain walls (that is, very sharp transitions between stripes with opposite magnetization orientations) and can be properly modelled by the domain approach of Kittel [7], such as in the work of Kooy and Enz [8]. In the beginning, this approach was employed to investigate bubble materials such as Ba-ferrite or Yttrium-Iron garnet plates, in which, when approaching magnetic saturation, stripe domains become energetically competitive with magnetic bubbles. The latter are cylindrical domains with high mobility that were explored for magnetic recording [8, 9, 10, 11]. Similar stripe domain patterns were later found in other thin film materials with high PMA, such as Co ultrathin layers on Au, FePt thin films and Co/Pt(Pd) multilayers [12, 13, 14, 15]. Several works have modelled the domains in these thin films, starting from the domain theory of [7, 8] and extending it to magnetic multilayers [16] or exploring limiting cases, such as the ultrathin layer regime [17].

Stripe domains also occur in systems with moderate or low PMA, i.e., with $Q < 1$, but above a critical thickness t_{cr} which in general depends on Q [6]. (Note that, for $Q \ll 1$, an approximate analytical estimate [18] is $t_{cr} = 2\pi\sqrt{A_{ex}/K_{PMA}}$, where A_{ex} is the exchange energy per unit length.) These "weak" stripe domains appear as dense, straight stripes with wide domain walls, that is, with smooth variation of the magnetization profile between stripes with opposite magnetizations. Since the PMA contribution to the magnetic free energy is in this case comparable with the

magnetostatic contribution, rigorously a micromagnetic approach is required to correctly model the behaviour of the system [6]. In order to interpret experimental data in real systems, convenient approximations to a fully three-dimensional (3D) micromagnetic model can be adopted. Typically, within such approaches the magnetostatic interaction associated with the stripe pattern is properly evaluated by taking into account a realistic, although simplified, magnetization profile across the stripes, such as in [19, 18, 20, 21, 22, 23, 24] (1D models), and/or across the film thickness, such as in [25, 26] (2D models). Alternatively, numerical micromagnetic calculations can be performed, but the limitation of such an approach is related to the finite size of the film plane [27, 28, 29, 30, 31].

Weak stripe domains were first predicted theoretically [32, 33] and later discovered experimentally in NiFe films [19, 34]. In the following years, the phenomenon has been found and deepened in different kinds of thin films with moderate PMA, such as FeGa [35, 36, 37, 38], FeN [39, 40, 31], FeSiB [41, 42], CoFeB [43], FeTaN [44], GdFe [45], NdCo [46], FeCoZr [23], $La_xSr_{1-x}MnO_3$ [47] and multilayers with moderate perpendicular anisotropy [48, 49, 50]. Very recently, it has been shown [51] that the formation of stripe domains can be induced in a Py film, even far below the critical thickness, coupling the Py film to a NdCo one, characterized by a moderate PMA.

The subject is currently attracting wide interest, thanks to the central role played today by magnetic thin films with PMA in many applications, from memories to logic devices and sensors [52]. Current active research on PMA films and multilayers is focused onto the definition of magnetic phase diagrams into different systems where magnetic stripe and skyrmion or bubble phases compete [47, 53, 54, 55, 56, 57, 50, 30]. Nanoscale magnetic textures are today the focus of a wide area of research, thanks to the possibility of generating and controlling the propagation of domains, bubbles, skyrmions and other kinds of spin textures for realising, e.g., logic circuits, racetrack memories, sensors and rf devices [58, 59, 60, 61]. Different methods have been pursued for the generation and controlled propagation, including magnetic field, electric current, electric field or mechanical stress [62, 56, 63, 59, 64, 65, 66]. In some cases, the geometry and local asymmetries of stripe domain patterns have been used to guide the propagation of skyrmions or bubbles [66, 67]. Other technological concepts are based on the controlled propagation of spin waves in films and micro/nanostructures through various kinds of spin textures. Notable examples are magnonic waveguides and spin-wave filters exploiting domain walls or different types of nanoscale spin textures [68, 69, 70, 71, 72, 73]. Moreover, recent studies showed that stripe domains can be used to control spin-wave propagation, by changing the relative orientation between the spin-wave wave vector and the domains axis [74, 75], suggesting the possibility to exploit stripe domains to realize reconfigurable spin-wave devices.

The present work is devoted to the experimental and theoretical investigation of the peculiar phenomenon shown by weak stripe domains [19] in a thin ferromagnetic film when a dc magnetic field is applied in the film plane along the direction perpendicular to the stripes axis: namely, the stripe domains reorientation taking place abruptly

above a threshold value for the transversal field. We focus on bct α'-Fe_8N_{1-x} thin films obtained by N_2^+irradiation of α-Fe films epitaxially grown on ZnSe/GaAs(001). First we show that the PMA strength of the Fe-N samples can be tuned by using different ion implantation and heat treatment conditions (while, in previous experimental studies of Fe-N films [39, 40, 31], the PMA was constant). This PMA gives rise to weak stripe domains, which we have visualized at remanence by magnetic force microscopy. Using this technique and vibrating sample magnetometry, we have proved the existence of a threshold field for the stripe domains reorientation in a transversal magnetic field. Noticeably, the threshold field increases on increasing the PMA of the Fe-N samples.Adopting a 1D model [19] of the magnetic stripe domains, where the essential parameter is the maximum canting angle of the stripe magnetization out of the film plane, the various contributions to the magnetic energy have been separately calculated in the presence of an in-plane magnetic field. The advantage of the 1D model is that it provides a mechanism for the abrupt stripe reorientation, and a clear evidence for the linear dependence of the reorientation threshold field on the PMA. Finally, the 1D model allows us to calculate another peculiar property of weak stripe domains, the so-called "rotatable" anisotropy [76, 77, 20, 78, 79]. The latter strongly affects the magneto-dynamic properties of the thin films [79, 37], providing an energy barrier which prevents from the free in-plane rotation of the magnetization vector. We show that the rotatable anisotropy increases linearly with increasing the PMA, in qualitative agreement with experimental data in our Fe-N films, and in other thin films with weak stripe domains [42, 80, 81]. In addition, a linear correlation between the rotatable anisotropy field and the threshold field for stripe reorientation has been established, confirming that both phenomena are driven by the PMA, responsible for the onset of weak stripe domains.

2. Experimental results

2.1. Materials and methods

A body-centered cubic (bcc) α-Fe thin film with a thickness of 78 nm was epitaxially grown on a ZnSe-buffered GaAs (001) substrate by molecular beam epitaxy (MBE). The main in-plane crystallographic directions attested by reflection high-energy electron diffraction measurements are α-Fe[110]‖ZnSe[110]‖GaAs[110] and α-Fe[100]‖ZnSe[100]‖GaAs[100]. Then, the film was *in situ* protected against oxidization with an 8-nm-thick gold capping layer. Four different samples have been prepared performing ion implantation of four pieces of this iron film, following the procedure detailed in our previous study [39]. Three samples were implanted with N_2^+ ions accelerated to 26 keV with fluences of 3.0×10^{16} N_2^+/cm^2 and 3.5×10^{16} N_2^+/cm^2, and 40 keV with a fluence of 5.3×10^{16} N_2^+/cm^2, respectively. The last sample was implanted with N_2^+ ions accelerated to 40 keV with a fluence of 5.3×10^{16} N_2^+/cm^2, and has undergone heat treatment at 150 °C for 72 h, in an ultra-high vacuum chamber.

X-ray diffraction (XRD) measurements were carried out using monochromatized

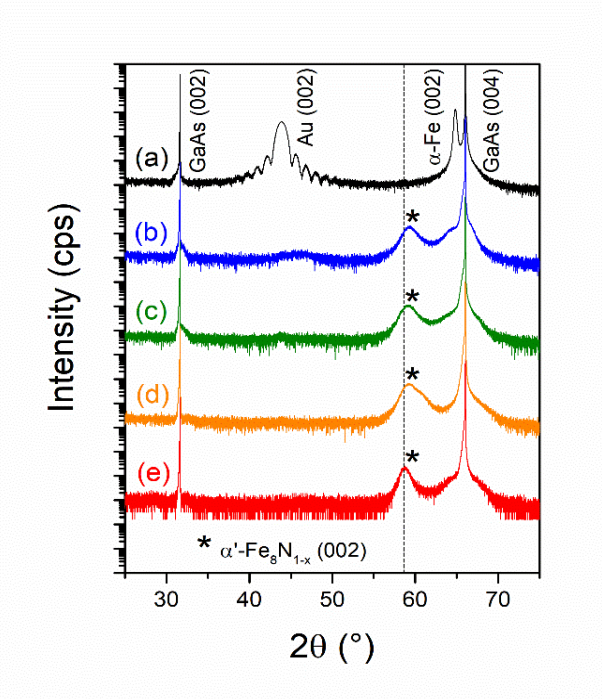

Figure 1. XRD patterns (θ-2θ) of the investigated samples: the as-grown sample (a); the as-implanted samples with a fluence of 3.0×10^{16} N_2^+/cm^2 at 26 keV (b); 3.5×10^{16} N_2^+/cm^2 at 26 keV (c); 5.3×10^{16} N_2^+/cm^2 at 40 keV (d) ; 5.3×10^{16} N_2^+/cm^2 at 40 keV, and the heat-treated sample implanted with a fluence of 5.3×10^{16} N_2^+/cm^2 at 40 keV (e). The black dashed line indicates the expected angle of the α'-Fe_8N_{1-x} (x = 0) (002) peak.

Cu K_α radiation in order to investigate the crystalline structure of the Fe-N films. The magnetization versus field of the samples was measured at room temperature by a vibrating sample magnetometer (VSM). A magnetic force microscope (MFM) was used to image the weak stripe domains of the magnetic thin films (phase detection).

2.2. Results and discussion

2.2.1. Structural investigations The out-of-plane XRD patterns of as-grown and implanted samples are reported in figure 1. For the unimplanted sample, the α-Fe(002) line is coherent with the epitaxial conditions given above (subsection 2.1).

After nitrogen implantation, out-of-plane XRD patterns disclose the presence of the body-centered tetragonal (bct) α'-Fe_8N_{1-x} phase. No reflections of α'-Fe_8N_{1-x} other than the one related to (002) crystal planes were observed. Hence, the c-axis of this bct compound is preferentially perpendicular to the film plane. Following the Bragg's law, the c-lattice constant of α'-Fe_8N_{1-x} can be inferred considering the 2θ angle of maximum intensity of the (002) diffraction peaks. For the as-implanted samples, we found $c \approx 3.12$ Å. For the heat-treated sample, we found $c \approx 3.14$ Å, which equals the

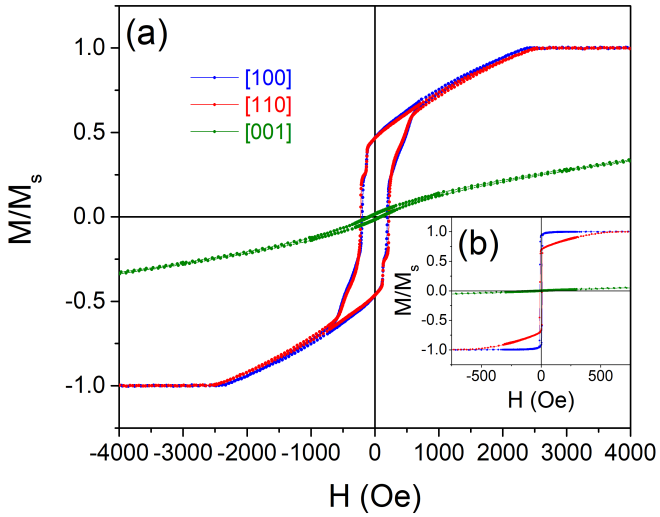

Figure 2. Magnetization curves for (a) the as-implanted iron thin film with 3.0×10^{16} N_2^+/cm^2 at 26 keV and (b) the as-grown iron thin film, measured by VSM. The field was applied along the out-of-plane [001] direction, the in-plane [100] and [110] directions.

expected value for α'-Fe_8N_{1-x} ($x = 0$) [82]. The increase of the c-lattice constant of α'-Fe_8N_{1-x} (previously formed by nitrogen implantation in our case) by a subsequent heat treatment is in agreement with previous studies [82]. Moreover, additional in-plane XRD measurements along the [100] and [110] directions of one of these samples (i.e., the one implanted with fluence 5.3 $\times10^{16}$ N_2^+/cm^2 at 40 keV) showed that the a-lattice constant of α'-Fe_8N_{1-x} is approximately equal to that of α-Fe, as expected [82]. Besides, the peak width of α'-Fe_8N_{1-x} possibly reflects its low crystallinity and the variation of its c-lattice constant. The small shoulder around $2\theta = 64°$ in the spectrum (b) of figure 1 can be attributed to a minor fraction of α-Fe in the film irradiated with the lowest fluence and energy. This is due to a slight variation of the nitrogen concentration through the film thickness, according to TRIM simulations [83]. Furthermore, the nitrogen distribution is probably impacted by the heat treatment conditions, through diffusion.

2.2.2. Magnetic measurements Figure 2 compares the magnetization curves for the as-implanted iron thin film with fluence of 3.0×10^{16} N_2^+/cm^2 at 26 keV and the as-grown iron thin film in the inset. Measurements were made along the in-plane [100] and [110] directions, and the out-of-plane [001] one. For the unimplanted sample, figure 2(b), we found the typical behaviour of a bcc iron film, with the easiest axis along the [100] in-plane direction, due to the magnetocrystalline anisotropy, and the hardest axis along the [001] out-of-plane direction because of the thin film shape anisotropy. Whereas, the in-plane hysteresis loops are quasi isotropic (i.e., nearly independent of the applied field orientation) and with a normalized in-plane remanence, $M_r/M_s \approx 0.5$, substantially smaller than for the unimplanted sample. Moreover, the in-plane loops

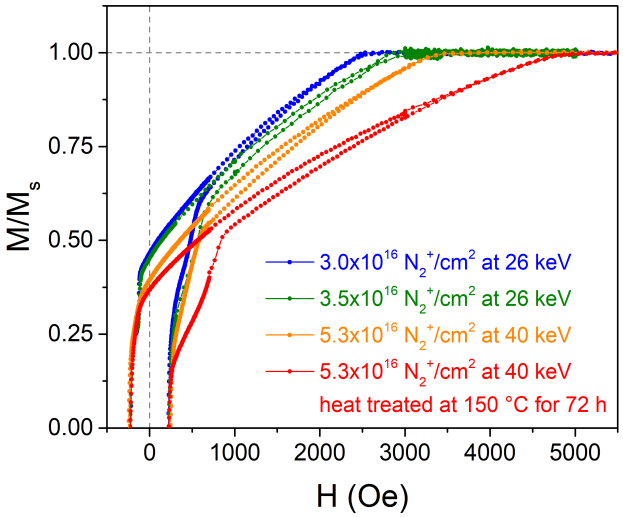

Figure 3. Comparison of in-plane magnetization curves of all the investigated Fe-N thin films, taken along the direction [110].

present a characteristic "transcritical shape" [84]: namely, an intermediate-field region exists, where the magnetization linearly depends on the intensity of the in-plane applied magnetic field. This behaviour is commonly regarded [19, 36] as a fingerprint of weak stripe domain structures, and it has been observed for all the Fe-N thin films investigated in this work. The out-of-plane hysteresis loop has a nearly zero remanence owing to the presence of the stripe domains. Nevertheless, we note that the specific in-plane magnetic properties vary depending on the preparation conditions of the samples, as shown in figure 3. More precisely we observed that, on increasing the ions energy and fluence, the in-plane saturation field increases, while the normalized in-plane remanence decreases, suggesting an increase of the PMA arising from the magnetocrystalline anisotropy of α'-Fe_8N_{1-x}. In addition, the annealing procedure was found to induce a further increase of the PMA strength. The value of K_{PMA} has been quantitatively estimated by measuring the area between the magnetization curves with the field along the in-plane and out-of-plane directions. We obtained K_{PMA} in the range from 5 to 7×10^6 erg/cm^3 (see figure 7(c) later on), consistent with the reported values for the magnetocrystalline anisotropy of α'-Fe_8N_{1-x} [85, 86], and in agreement with K_{PMA} values measured by ferromagnetic resonance [87]. We note that, assuming $M_s = 1700$ emu/cm^3 [31], the quality factor Q of the Fe-N samples investigated in this work is between 0.275 and 0.385, depending on the preparation conditions, while the critical thickness above which the stripe domains appear is about 40 nm.

In figure 4, the presence of weak stripe domains at remanence in the as-implanted iron thin film with 3.0×10^{16} N_2^+/cm^2 at 26 keV is revealed by MFM. We observed very regular stripe domains, aligned along the in-plane direction of the last saturating magnetic field, and having a period of 110-140 nm. Similar stripe domain patterns have

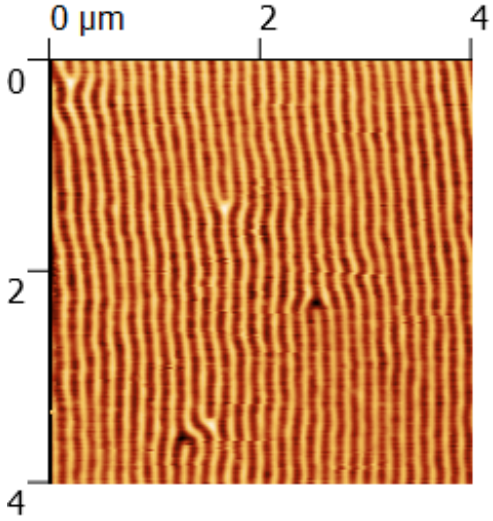

Figure 4. MFM image of the as-implanted iron thin film with 3.0 $\times 10^{16}$ N_2^+/cm^2 at 26 keV, revealing the weak stripe domains at remanence. The magnetic stripes are aligned along the [110] direction of GaAs.

been found for the other samples. In particular, the stripes period was observed to be almost independent of the ions implantation parameters.

Furthermore, we carried out a detailed MFM study of the stripe domain reorientation when a dc magnetic field is applied in-plane along a direction perpendicular to the stripes axis. The MFM measurements (figure 5) were performed in the as-implanted sample with a fluence of 5.3×10^{16} N_2^+/cm^2 at 40 keV. The stripes were initially aligned along the [100] direction, then an in-plane magnetic field, H_{trans}, was applied perpendicularly to the stripes axis and its maximum value H_{trans}^{max} was progressively increased. Each image was recorded at remanence. The dark/white dots in figure 5 highlight the presence of magnetic edge dislocations, namely topological defects spontaneously nucleated in the stripe domain structure [39]. We observed that the whole stripe structure remains unperturbed up to $H_{trans}^{max} = 800$ Oe (not shown). For $H_{trans}^{max} = 1000$ Oe, the stripes were found to coherently rotate by a rather large angle ($\alpha_0 \approx 60°$) towards the direction of the applied field, apart from a small region where the straightness of the domains is not preserved (see figure 5(b)). For higher values of H_{trans}^{max} the stripe domains continued their reorientation, which appeared to be completed at the saturation field ($H_{trans}^{max} = 4000$ Oe, see figure 5(d)). Note that, in each panel of figure 5, the dark/white contrast of the MFM image is the same irrespective of H_{trans}^{max}, because each MFM image has been recorded *at remanence*. On the contrary, whenever MFM images are recorded *in the presence* of an in-plane dc magnetic field, a progressive loss of contrast is observed [88, 89, 90] with increasing the field intensity, because the in-plane component of the film magnetization progressively increases.

In order to better understand the reorientation process, VSM measurements have been performed applying a transversal magnetic field, H_{trans} along the in-plane direction perpendicular to the stripes axis. All the Fe-N samples obtained from the same 78-nm-

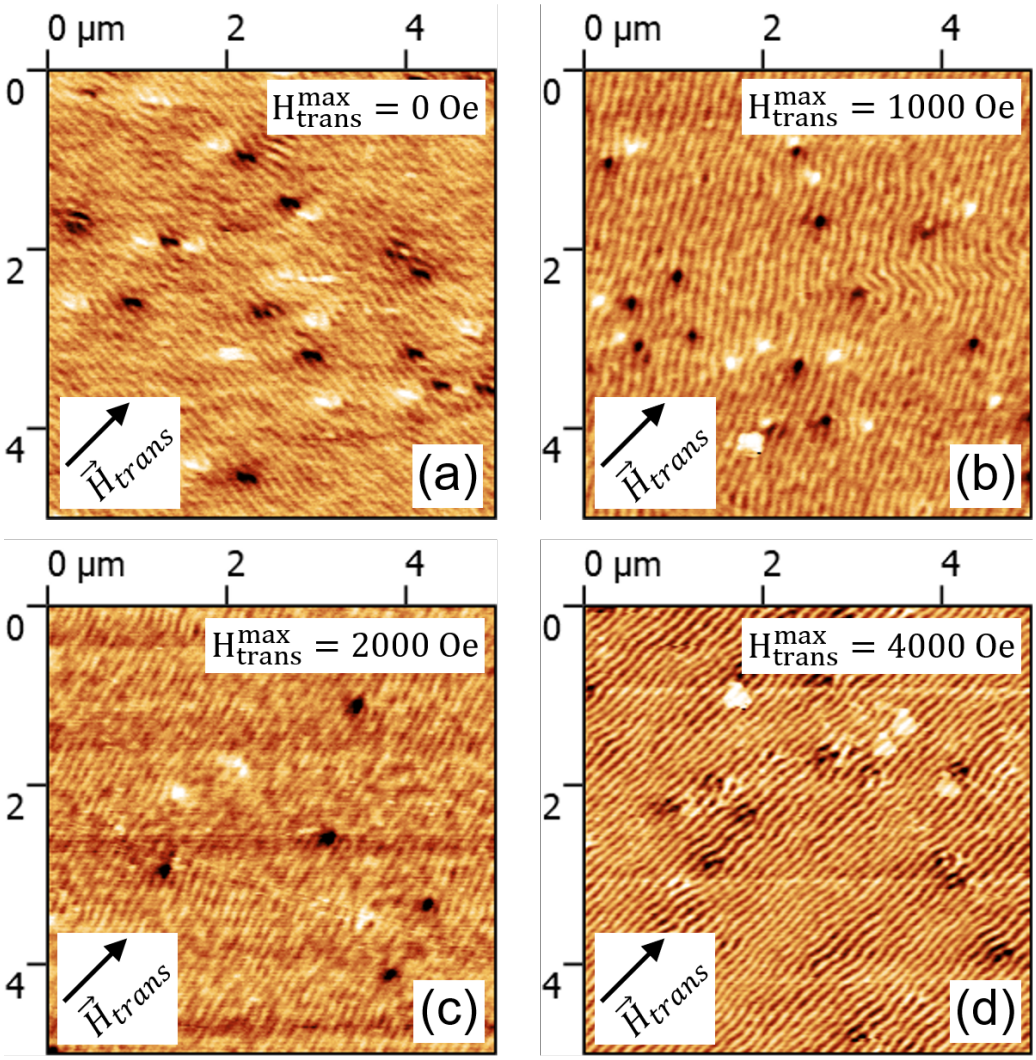

Figure 5. (Color online) MFM images of the stripe domains, recorded at remanence in the as-implanted sample with a fluence of 5.3×10^{16} N_2 /cm^2 at 40 keV. The stripes were aligned initially along the [100] direction, then a magnetic field H_{trans} was applied in plane perpendicularly to the stripes axis. For each panel, the field intensity was increased up to H^{max}_{trans}, then the field was removed, and the MFM image was recorded at remanence.

thick iron film, differing (see figure 1) for technical specifications of ion implantation and heat treatment, were investigated. For each sample, a saturating field was first applied in plane to align the stripe domains along the [110] direction and was removed. Then, a transversal field, H_{trans}, was applied in plane perpendicularly to the stripe axis, and reduced to zero while the magnetization component along the direction of H_{trans} was recorded. Following the procedure described in [39], this two-step measurement was repeated many times, each time increasing the maximum value of the transversal field, H^{max}_{trans}, up to reach the in-plane saturation field, H_s. For each value of H^{max}_{trans}, the component of the magnetization parallel to the direction of the magnetic field versus H_{trans} has been measured both in applied field (M_{ON}/M_s) and at remanence

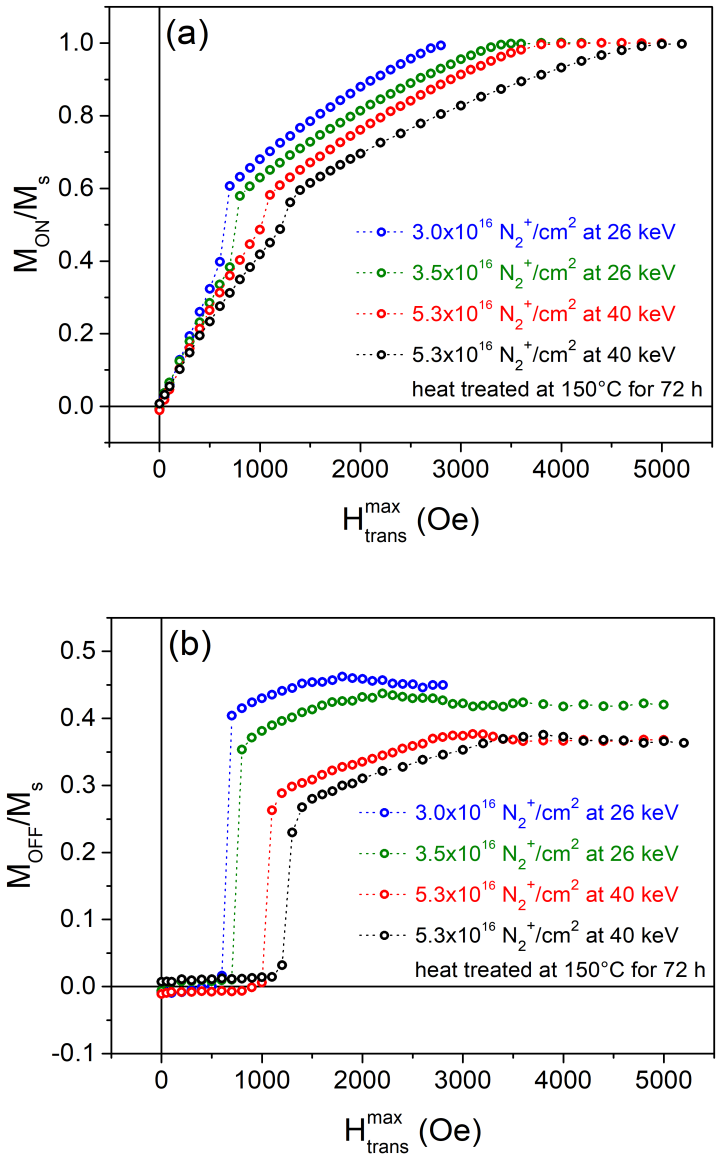

Figure 6. (Color online) Evolution of the normalized magnetization component, measured by VSM along the magnetic field applied in plane perpendicularly to the stripe axis, either in the presence of the field (a), or at remanence (b), as a function of the maximum value of the transversal field, for all the investigated Fe-N films.

(M_{OFF}/M_s), as shown in figure 6(a) and 6(b), respectively. In agreement with previous work [39], a threshold value, H^{thr}_{trans}, is found for the maximum transversal field, H^{max}_{trans}, as indicated by the sharp change of both M_{ON}/M_s and M_{OFF}/M_s, and which is consistent with the rotation threshold of the stripe domain pattern. Comparing figure 6(a) and 6(b), it appears that the in-field magnetization, M_{ON}/M_s, and the remanent magnetization, M_{OFF}/M_s, exhibit a different behaviour versus H^{max}_{trans}. For $H^{max}_{trans} < H^{thr}_{trans}$, when the orientation of the stripe domains doesn't change, M_{ON}/M_s

is found to increase, while M_{OFF}/M_s remains almost zero. For $H^{max}_{trans} > H^{thr}_{trans}$, when the stripe domains start to rotate, both M_{ON}/M_s and M_{OFF}/M_s are found to increase, evidencing the start of the irreversible process.

As shown in figure 6, even if the four investigated samples exhibit a similar behaviour, they are characterized by a different value of the threshold field H_{thr}. In Figure 7, the threshold field for stripe reorientation is plotted as a function of the in-plane saturation field, H_s, the normalized in-plane remanence, M_r/M_s, and the perpendicular magnetic anisotropy energy density, K_{PMA}, for the four investigated Fe-N thin film samples. These findings clearly show that the threshold field for stripe reorientation linearly increases with the PMA, in accordance with the work by Coïsson et al [42], where such linear dependence has been observed for stripe domains in $Fe_{78}Si_9B_{13}$ thin films.

3. One-dimensional model of stripe domains

In order to explain the linear dependence of the reorientation threshold field (H^{thr}_{reor}) as a function of the in-plane saturation field (H_s) experimentally observed in our Fe-N films, as well as in other magnetic films (FeSiB [42]) with weak stripe domains, we adopt a 1D model of the stripe domain structure originally proposed by Saito *et al.* [19] for Permalloy films. In principle, a micromagnetic approach [6] would be required in order to correctly model the behaviour of weak stripe domains. However, it is very difficult to investigate the peculiar phenomenon of stripe reorientation in a transversal magnetic field using numerical micromagnetic calculations, owing to the strong pinning effects induced by the finite size of the film plane exploited in the simulations. As it is explained in more detail in Appendix A, where different 1D models for stripe domains are compared, the advantage of the Saito model [19] is that it allows one to obtain approximate analytical expressions for the magnetic energy contributions. In this way, it is easy to understand the role of the model parameters in the stripe domains reorientation, induced by a transversal magnetic field above a threshold value.

The 1D stripe domain structure is sketched in figure 8. The stripes are assumed to be infinite along the y direction of the film plane, xy. Consequently the magnetization, $\mathbf{M}$, depends only on x, the in-plane direction perpendicular to the stripes axis. Hereafter y will be denoted as the longitudinal direction, and x as the transversal direction. The magnetization $\mathbf{M} = (M^x, M^y, M^z)$ forms an angle $\theta(x)$ with the film plane, while the in-plane projection, $\mathbf{M}^{IP} = (M^x, M^y)$, forms an angle φ_0, independent of x, with the stripes axis y. One has therefore

$$\mathbf{M}(x) = M_s\Big(\cos\theta(x)\sin\varphi_0, \cos\theta(x)\cos\varphi_0, \sin\theta(x)\Big) \tag{1}$$

The angle $\theta(x)$ is assumed [19] to be a periodic function of x, with the 1D profile (sketched in figure 8(c))

$$\theta(x) = (-1)^n \, \frac{(x - nd)}{d} \, 2\theta_0, \qquad \text{for} \;\; |x - nd| \leq \frac{d}{2} \quad (n = 0, 1, 2, \cdots) \tag{2}$$

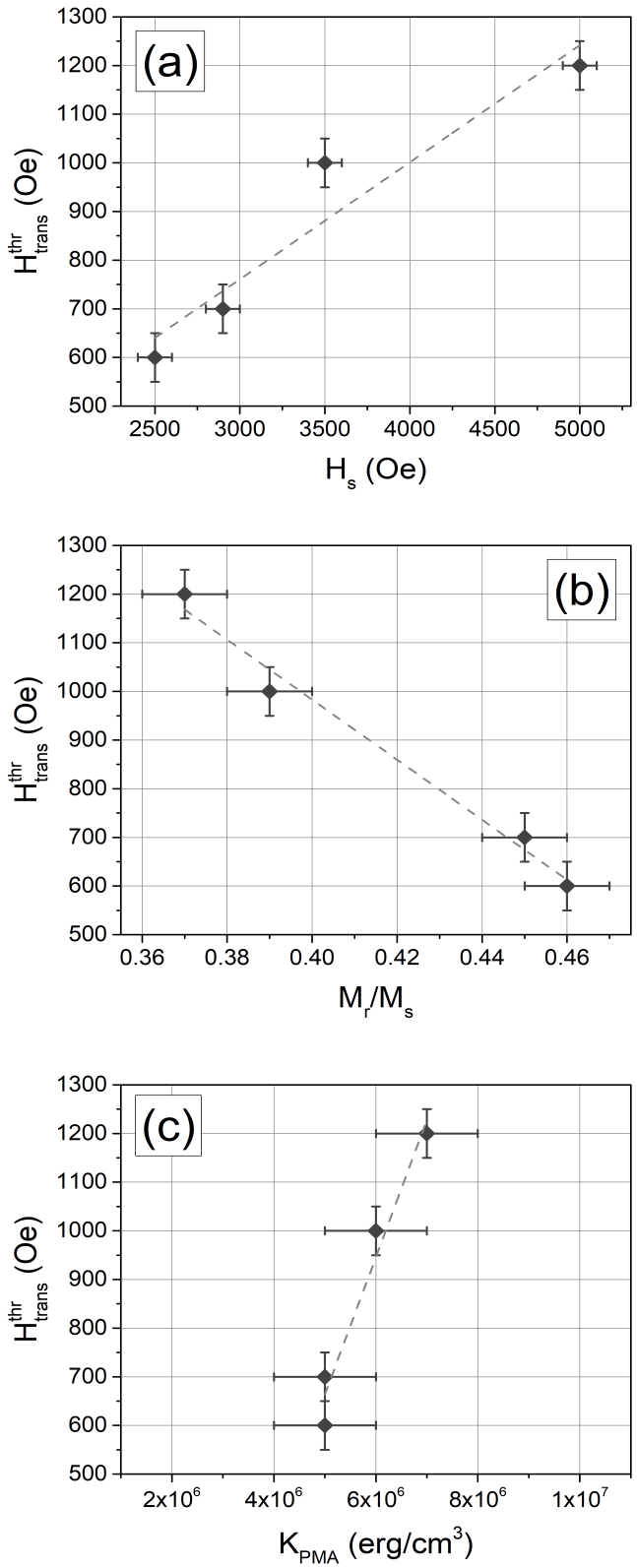

Figure 7. The measured threshold field for stripe domains reorientation, plotted versus (a) the in-plane saturation field; (b) the normalized in-plane remanence; (c) the perpendicular magnetic anisotropy, for the series of Fe-N thin films in figure 6. The grey dashed lines are guides to the eye.

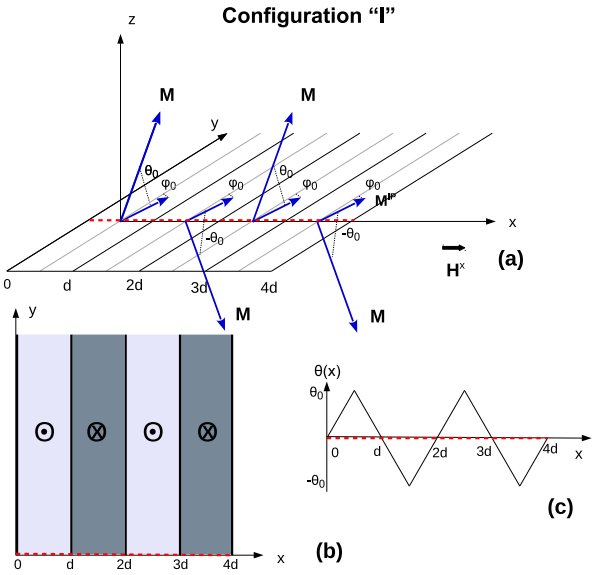

Figure 8. The one-dimensional model of the magnetic stripe domains [19] adopted in this work. (xy is the film plane, and y is the direction of the stripes axis at remanence; the film thickness is not shown.) A possible configuration of the film magnetization in a transversal magnetic field $\mathbf{H} = (H^x, 0)$ of small intensity: (a) Perspective view of the film surface. The magnetization $\mathbf{M}(x)$ forms an angle $\theta(x)$ with the film plane, periodically alternating in sign along the red dashed line. The uniform in-plane magnetization $\mathbf{M}^{IP}$ forms a constant angle φ_0 with y. (b) Top view of the "up-down" magnetic stripe domain pattern with period $P = 2d$ (d = stripes width). (c) The triangular profile of the out-of-plane canting angle $\theta(x)$ [19].

where d is the stripes width and $P = 2d$ is the period; θ_0 denotes the maximum value assumed by the out-of-plane canting angle $\theta(x)$ along the transversal direction, x.
The total energy density, ϵ_{tot}, is the sum of different magnetic contributions

$$\epsilon_{tot} = \epsilon_A + \epsilon_K + \epsilon_M + \epsilon_H \tag{3}$$

The contribution, ϵ_A, of the exchange interaction, A_{ex}, is

$$\epsilon_A = \frac{A_{ex}}{P}\int_{-\frac{P}{2}}^{\frac{P}{2}}\left[\left(\frac{d\theta}{dx}\right)^2\right) + \left(\frac{d\varphi_0}{dx}\right)^2\cos^2\theta(x)\Big]dx = \frac{A_{ex}}{2d}\int_{-d}^{d}\left(\frac{d\theta}{dx}\right)^2 dx = \frac{4A_{ex}\theta_0^2}{d^2} \tag{4}$$

The uniaxial contribution, ϵ_K, comes from the perpendicular magnetic anisotropy, $K_{PMA} > 0$, which favours (see figure 8(a)) the out-of-plane direction, z

$$\epsilon_K = -\frac{K_{PMA}}{P}\int_{-\frac{P}{2}}^{\frac{P}{2}}\sin^2\theta(x)dx = -\frac{K_{PMA}}{2}\left[1 - \frac{\sin(2\theta_0)}{2\theta_0}\right] \tag{5}$$

In order to calculate the contribution of the magnetostatic energy, ϵ_M, we exploit an approach by Corciovei and Adam [91], which is valid even for a 2D periodic domain structure. Inside the film, the magnetization vector is expanded in Fourier series

$$\mathbf{M}(\mathbf{r}) = \sum_{\mathbf{k}} \mathbf{M}_{\mathbf{k}}(z)e^{i\mathbf{k}\cdot\mathbf{r}^{IP}} \tag{6}$$

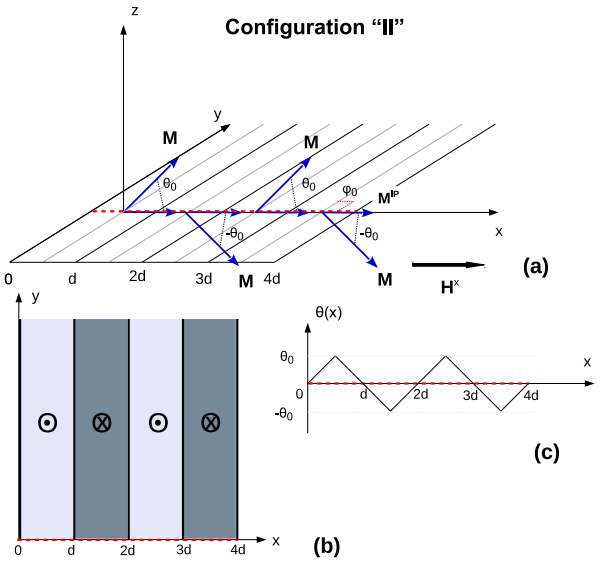

Figure 9. (Color online) A possible configuration of the film magnetization in a transversal magnetic field $\mathbf{H} = (H^x, 0)$ of moderate intensity. The direction of the stripes axis is the same as in zero field (y), but the in-plane magnetization $\mathbf{M}^{IP}$ has rotated by an angle $\varphi_0 = 90°$, so as to become parallel to the direction of the applied field (x). (a) (b) (c) are defined as in figure 8. The stripes width d is assumed not to depend on H^x.

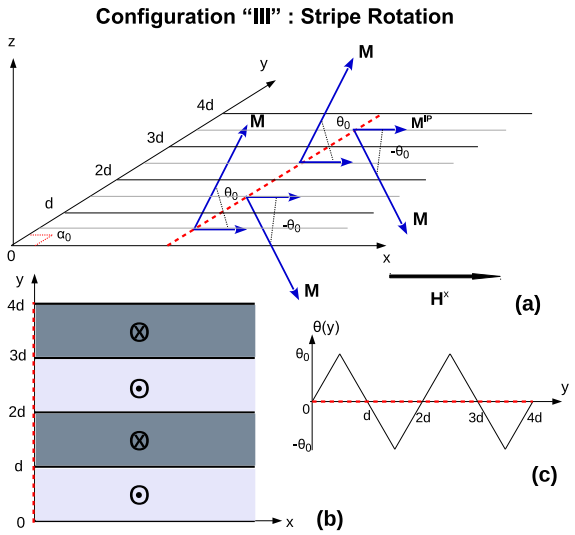

Figure 10. (Color online) A possible equilibrium magnetization configuration in a transversal magnetic field $\mathbf{H} = (H^x, 0)$ of high intensity. The applied field is strong enough so as to rotate the direction of the stripes axis by an angle $\alpha_0 = 90°$ with respect to the zero-field direction (y). The in-plane magnetization $\mathbf{M}^{IP}$ is parallel to the direction of the applied field (x) due to the absence of in-plane magnetocrystalline anisotropies. (a) (b) (c) are defined as in figure 8. The stripes width d is assumed not to depend on H^x.

where, in general, the position vector is $\mathbf{r}^{IP} = (x, y, 0)$, and the wavevector is $\mathbf{k} = (k_x, k_y, 0) = 2\pi\Big(\frac{n_x}{P}, \frac{n_y}{P}, 0\Big)$. P is the period of the domain pattern within the film plane, and $n_x, n_y = 0, \pm 1, \pm 2, \cdots$. Outside the film, one has $\mathbf{M}(\mathbf{r}) = 0$. Next, the magnetostatic energy can be separated [91] into a surface and a volume contribution, $\epsilon_M = \epsilon_S + \epsilon_V$. Making the approximation, valid for not too thick films, that the magnetization does not depend on the perpendicular coordinate, z, the two contributions take the form [91], respectively

$$\epsilon_S = 2\pi\Big(\mathbf{i}_z \cdot \mathbf{M}_0\Big)^2 + 2\pi \sum_{\mathbf{k}\neq 0} \Big(\mathbf{i}_z \cdot \mathbf{M}_{\mathbf{k}}\Big)\Big(\mathbf{i}_z \cdot \mathbf{M}_{-\mathbf{k}}\Big)\frac{(1 - e^{-kt})}{kt} \tag{7}$$

$$\epsilon_V = 2\pi \sum_{\mathbf{k}\neq 0} \Big(\mathbf{k}_0 \cdot \mathbf{M}_{\mathbf{k}}\Big)\Big(\mathbf{k}_0 \cdot \mathbf{M}_{-\mathbf{k}}\Big)\Big[1 - \frac{(1 - e^{-kt})}{kt}\Big] \tag{8}$$

where t denotes the film thickness, $\mathbf{k}_0$ is the unit vector along $\mathbf{k} = (k_x, k_y, 0)$, and $\mathbf{i}_z$ the unit vector along z. Specializing to the case of the 1D stripe domain structure in figure 8 and equation (2), one has $k_y = 0$ because the stripes are infinite along y. It then follows that $\mathbf{k} = \Big(\frac{2\pi n}{P}, 0, 0\Big)$, where now P is the period of the stripes and $n = 0, \pm 1, \pm 2, \cdots$. The magnetization components ($\alpha = x, y, z$) are

$$M^\alpha(x) = \sum_k M_k^\alpha e^{ikx}, \;\; k = \frac{\pi n}{d} \qquad (n = 0, \pm 1, \pm 2, \cdots) \tag{9}$$

where $d = P/2$ is the stripes width, and

$$M_k^\alpha = \frac{1}{P}\int_{-\frac{P}{2}}^{\frac{P}{2}} M^\alpha(x) e^{-ikx} dx = \frac{1}{2d}\int_{-d}^{d} M^\alpha(x) e^{-i\frac{\pi n x}{d}}\, dx \tag{10}$$

Taking (1) and (2) into account, the contributions (7) and (8) to the magnetostatic interaction ϵ_M can respectively be rewritten as

$$\begin{aligned}\epsilon_S &= 2\pi M_s^2 \sum_{n\neq 0} \Big[\frac{1}{2d}\int_{-d}^{d} \sin\theta(x) \sin\Big(\frac{\pi n x}{d}\Big) dx\Big]^2 \Big(\frac{d}{\pi n t}\Big)\Big(1 - e^{-\frac{\pi n t}{d}}\Big) \\ &= 4\pi M_s^2 \;\theta_0^2 \cos^2\theta_0 \sum_{n>0,\; n\; odd} \Big\{\frac{1}{[(\frac{n\pi}{2})^2 - \theta_0^2]^2}\Big(\frac{d}{\pi n t}\Big)\Big(1 - e^{-\frac{\pi n t}{d}}\Big)\Big\}\end{aligned} \tag{11}$$

$$\begin{aligned}\epsilon_V &= 2\pi M_s^2 \sum_{n\neq 0} \Big[\frac{1}{2d}\int_{-d}^{d} \cos\theta(x) \cos\Big(\frac{\pi n x}{d}\Big) dx\Big]^2 \Big[1 - \Big(\frac{d}{\pi n t}\Big)\Big(1 - e^{-\frac{\pi n t}{d}}\Big)\Big] \times \sin^2\varphi_0 \\ &= 4\pi M_s^2 \;\theta_0^2 \sin^2\theta_0 \sum_{m>0,\; m\; even} \Big\{\frac{1}{[(\frac{m\pi}{2})^2 - \theta_0^2]^2}\Big[1 - \Big(\frac{d}{\pi m t}\Big)\Big(1 - e^{-\frac{\pi m t}{d}}\Big)\Big]\Big\} \times \sin^2\varphi_0 \\ &= K_{rot} \times \sin^2\varphi_0\end{aligned} \tag{12}$$

Note that the volume contribution ϵ_V has been expressed, according to [20], in terms of an effective rotatable anisotropy, K_{rot}. Keeping only the $m = 2$ term in (12), the following estimate for K_{rot} is obtained

$$K_{rot} \approx 4\pi M_s^2 \;\frac{\theta_0^2 \sin^2\theta_0}{(\pi^2 - \theta_0^2)^2}\;\Big[1 - \frac{d}{2\pi t}\Big(1 - e^{-\frac{2\pi t}{d}}\Big)\Big] \tag{13}$$

The effective rotatable anisotropy field [20] H_{rot}, associated with K_{rot}, takes the form

$$H_{rot} = \frac{2K_{rot}}{\langle M_y(x)\rangle} \approx 8\pi M_s \, \frac{\theta_0^3 \sin\theta_0}{(\pi^2-\theta_0^2)^2} \, \frac{1}{\cos\varphi_0} \, \Big[1 - \frac{d}{2\pi t}\Big(1 - e^{-\frac{2\pi t}{d}}\Big)\Big] \tag{14}$$

where the average in-plane magnetization $\langle M^{IP}(x)\rangle$ is

$$\langle M^{IP}(x)\rangle = \frac{1}{P}\int_{-\frac{P}{2}}^{\frac{P}{2}} M_s \cos\theta(x) = M_s \frac{\sin\theta_0}{\theta_0} \tag{15}$$

and the three average magnetization components are

$$\langle M^x(x)\rangle = M_s \frac{\sin\theta_0}{\theta_0}\sin\varphi_0, \quad \langle M^y(x)\rangle = M_s \frac{\sin\theta_0}{\theta_0}\cos\varphi_0, \quad \langle M^z(x)\rangle = 0 \tag{16}$$

Note that, in the limit $\theta_0 \to 0$, one has $\langle M^{IP}\rangle/M_s \to 1$: i.e., the magnetization lies entirely in the film plane.

Finally, the Zeeman energy density, ϵ_H, namely the contribution from a dc magnetic field applied in plane along a direction forming an angle ψ with the stripes axis, y, is

$$\epsilon_H = -M_s H \frac{\sin\theta_0}{\theta_0}\cos(\psi - \varphi_0) \tag{17}$$

Once obtained the total energy density (3) as the sum of the various contributions (4), (5), (11), (12), and (17), the equilibrium values for the polar and azimuthal angles, θ_0^{eq} and φ_0^{eq} respectively, can now be determined by minimizing $\epsilon_{tot}(\theta_0, \varphi_0)$ with respect to its arguments. In the following, for simplicity we consider only two limiting cases, of a transversal magnetic field H^x ($\psi = 90°$) and a longitudinal magnetic field H^y ($\psi = 0°$)

$$\epsilon_{H,trans} = -M_s H^x \frac{\sin\theta_0}{\theta_0}\sin\varphi_0 \tag{18a}$$

$$\epsilon_{H,long} = -M_s H^y \frac{\sin\theta_0}{\theta_0}\cos\varphi_0 \tag{18b}$$

Our numerical calculations for the equilibrium configuration and the magnetic energy density are presented in section 4 and Appendix B for transversal field, and in Appendix C for longitudinal field, respectively. The calculations were performed by setting the material parameters equal to values obtained in previous investigations of the Fe-N films. The saturation magnetization is $M_s = 1700$ emu/cm^3 [39]. The exchange interaction is $A_{ex} = 1.8 \times 10^{-6}$ erg/cm [92]. The magnetocrystalline in-plane anisotropy was set to zero, while different values of the out-of-plane uniaxial anisotropy (with K_{PMA} ranging from 5.7 to 6.3 $\times 10^6$ erg/cm^3) were exploited, in order to investigate the role of the PMA in the stripe reorientation process. The film thickness is the same for all samples, $t = 78$ nm. Finally, the period of the stripes was kept constant, $P = 115$ nm. Such an approximation is in good agreement with experimental observations showing that, in many film systems (NiFe[19], FeGa [37, 38], FeN [39], and FeSiB [42]), the period of the stripe domains does not vary on changing the intensity of the in-plane applied field.

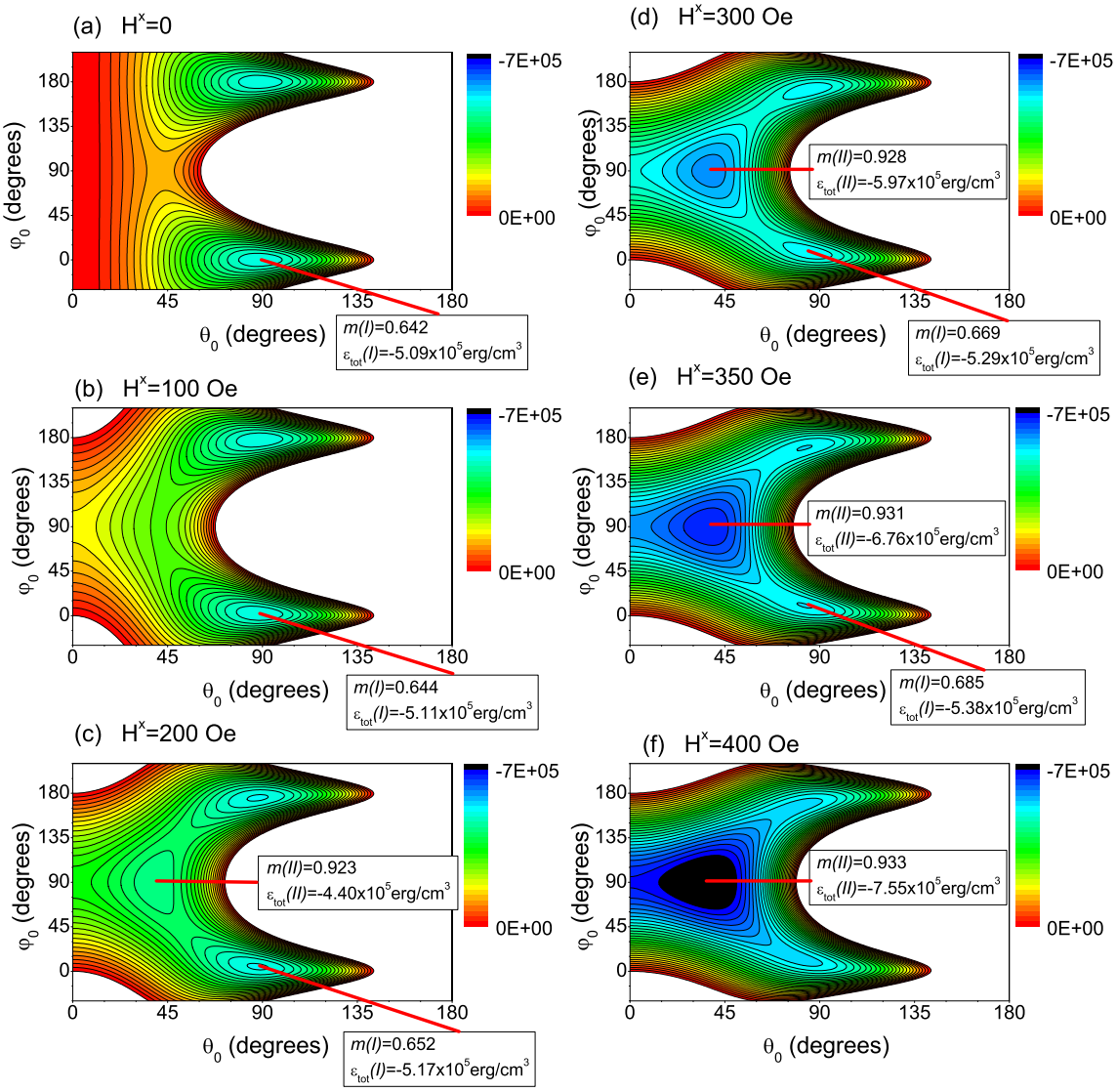

Figure 11. (Color online) Low field configurations I and II without stripe rotation ($\alpha_0 = 0°$). Contour plots of the total energy density $\epsilon_{tot}(\theta_0, \varphi_0)$ for different values of the transversal field intensity H^x. (a) H^x=0; (b) 100 Oe; (c) 200 Oe; (d) 300 Oe; (e) 350 Oe; (f) 400 Oe. In each panel, the box shows the values of the total energy density (19) in the minimum, and of the normalized in-plane magnetization $m = M_{IP}/M_s = (\sin\theta_0^{eq})/\theta_0^{eq}$. In the energy scale, the blue colour denotes low energy, while the red colour denotes high energy.

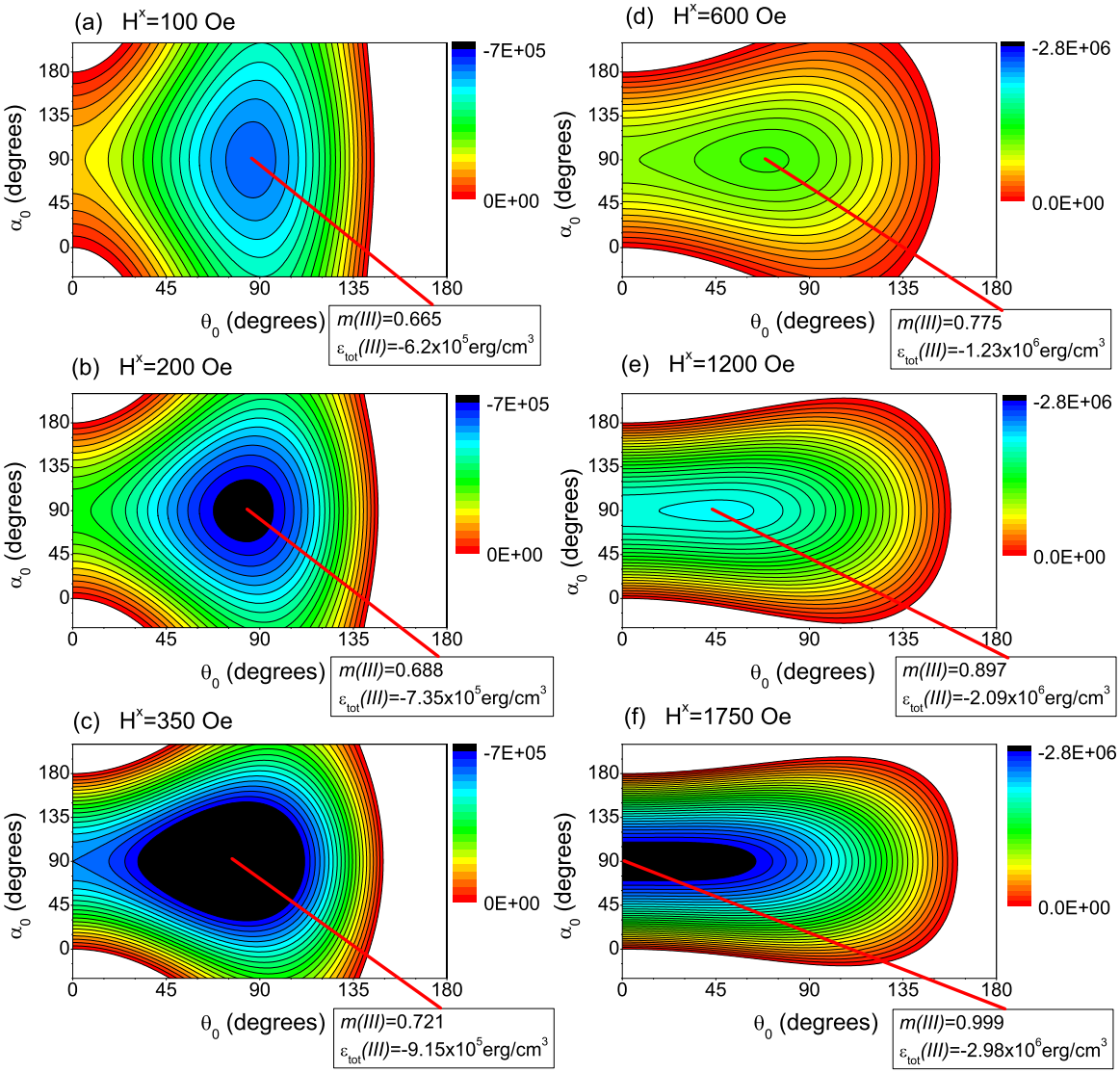

Figure 12. (Color online) High field configuration III with stripe rotation ($\alpha_0 = 90°$). Contour plots of the total energy density $\epsilon_{tot}(\theta_0, \alpha_0)$ for different values of the transversal field intensity H^x. (a) H^x=100 Oe; (b) 200 Oe; (c) 350 Oe; (d) 600 Oe; (e) 1200 Oe; (f) 1750 Oe (saturation field). In each panel, the box shows the values of the total energy density (19) in the minimum, and of the normalized in-plane magnetization $m = M_{IP}/M_s = (\sin\theta_0^{eq})/\theta_0^{eq}$. Please note that the energy scale in figure 12(a,b,c) is the same as in figure 11(a-f), but it is different from the energy scale in figure 12(d,e,f).

4. Mechanism of stripe domains reorientation in Fe-N thin films

The equilibrium configurations of the film magnetization when an external magnetic field is applied along the in-plane x direction, perpendicular to the stripes axis, y, have been calculated as a function of the field intensity, H^x. For increasing values of H^x, we hypothesize three configurations, schematically illustrated in figures 8, 9, and 10.

Low field configurations (I, II) without stripe rotation. For sufficiently low values of H^x, we look for two possible equilibrium configurations, I and II, both characterized by the direction of the stripes axis being y, i.e. the same as at remanence. In the configuration I (figure 8), the in-plane uniform canting angle, formed by the in-plane magnetization component $\mathbf{M}^{IP}$ with the stripes axis (y), is small: $\varphi_0 \ll 90°$. In contrast, in the configuration II (figure 9), the in-plane angle is exactly $\varphi_0 = 90°$: i.e., $\mathbf{M}^{IP}$ is completely rotated towards the direction of the applied field, but the axis of the up/down magnetic stripe domains is not rotated. Also the out-of-plane maximum canting angle θ_0 is expected to be different, in general, for the two configurations I and II. The total energy density is given by

$$\epsilon_{tot}(\theta_0, \varphi_0) = \epsilon_A + \epsilon_K + \epsilon_S + \epsilon_V + \epsilon_{H,trans}^{(I,II)} \tag{19}$$

where for both configurations I and II the various contributions on the r.h.s. of (19) are explicitly given by (4), (5), (11), (12), and (18a). By minimizing ϵ_{tot} with respect to its arguments, the equilibrium angles θ_0^{eq} and φ_0^{eq} are obtained.

In figure 11, the contour plots of $\epsilon_{tot}(\theta_0, \varphi_0)$ are reported for a fixed value ($K_{PMA} = 6.3 \times 10^6$ erg/cm^3) of the out-of-plane uniaxial anisotropy and selected values of the transversal field, H^x, ranging from 0 to 400 Oe. At $H^x = 0$ (figure 11(a)) and 100 Oe (figure 11(b)), the total energy density has only one minimum, with small in-plane uniform canting angle, $\varphi_0^{eq} \gtrsim 0$, and large out-of-plane maximum canting angle, $\theta_0^{eq} \lesssim 90°$, corresponding to the configuration I (figure 8). Consequently, both at H^x=0 and 100 Oe the normalized in-plane magnetization turns out to be sensibly smaller than 1 ($m = M_{IP}/M_s = (\sin\theta_0^{eq})/\theta_0^{eq} \sim 0.64$). At $H^x = 200$ Oe (figure 11(c)) one observes that, in addition to the minimum corresponding to the configuration I, a second minimum develops with $\theta_0^{eq} \sim 40°$ and $\varphi_0^{eq} = 90°$. The second minimum thus corresponds to the configuration of type II (figure 9), and it turns out to be higher in energy than the first. Note that at H^x=200 Oe the normalized in-plane magnetization is $m \approx 0.92$ for configuration II, thus sensibly larger than $m \approx 0.65$, the value for configuration I at the same field intensity. On further increasing H^x, the situation is reversed. In fact, at $H^x = 300$ Oe (figure 11(d)) and 350 Oe (figure 11(e)), the deeper minimum corresponds to the configuration II, and the shallower one to the configuration I. Eventually, at $H^x = 400$ Oe (figure 11(f)), the minimum corresponding to the configuration I disappears.

High field configuration (III) with stripe rotation. For sufficiently high values of H^x, we look for the equilibrium configuration III (Fig. 10), where the direction of the stripes

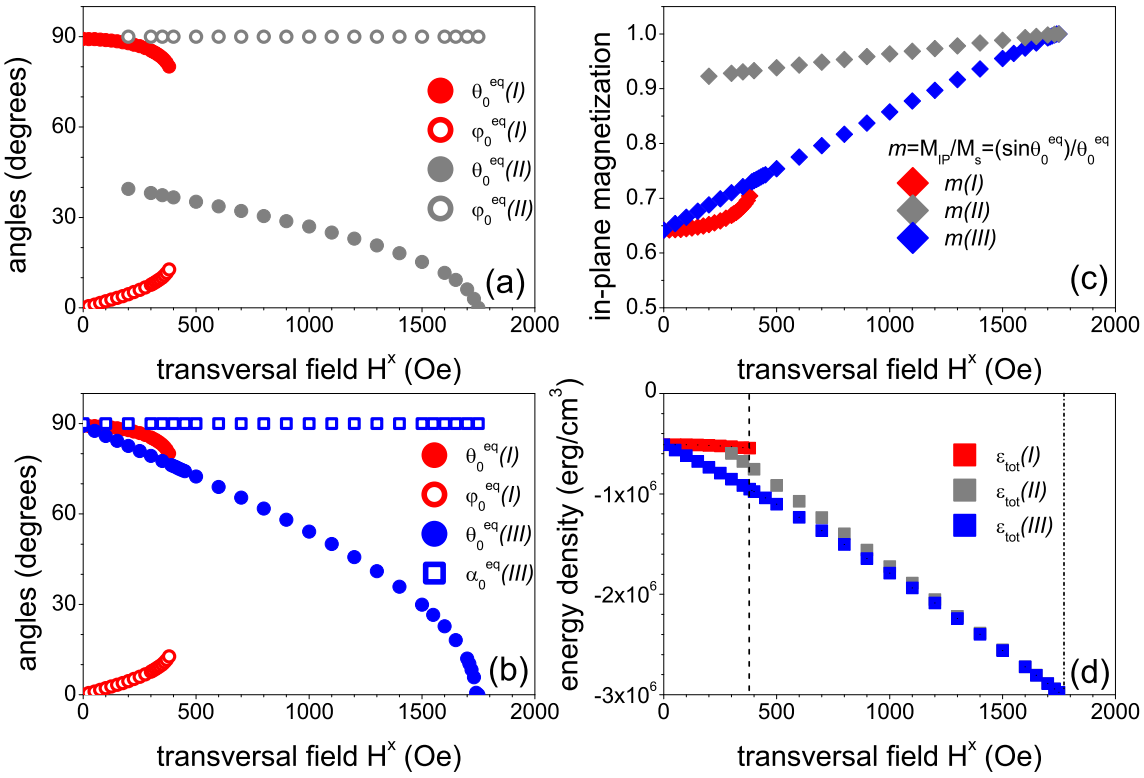

Figure 13. (Color online) The calculated configurations and magnetic energy density of the film versus the transversal field intensity, H^x. (a) and (b): The out-of-plane maximum canting angle, θ_0^{eq}, the in-plane uniform canting angle, φ_0^{eq}, and the stripe rotation angle, α_0^{eq}, calculated at equilibrium for different configurations, of type I (red symbols), type II (grey symbols) and type III (blue symbols), respectively. (c) and (d): The average in-plane magnetization, m, and the total energy density, ϵ_{tot}, calculated for the configurations I, II, and III. In (d), the vertical dashed line marks a possible abrupt transition from the metastable state I to the lowest energy state III at the reorientation threshold field ($H^{thr}_{trans} \approx 380$ Oe); the vertical short-dash-dotted line marks the position of the saturation field ($H_s \approx 1750$ Oe).

axis is rotated by a large angle α_0 with respect to y, the direction at remanence. The total energy density is now expressed as

$$\epsilon_{tot}(\theta_0, \alpha_0) = \epsilon_A + \epsilon_K + \epsilon_S + \epsilon_V + \epsilon^{(III)}_{H,trans} \tag{20}$$

The first four terms on the r.h.s. of equation (20) are respectively given by (4), (5), (11), and (12) where, in the absence of in-plane magnetocrystalline anisotropies, one can set $\varphi_0 = 0$. The fifth term is the transversal field contribution, namely the only one in (20) which contains an explicit dependence on α_0

$$\epsilon^{(III)}_{H,trans} = -M_s H^x \frac{\sin\theta_0}{\theta_0} \sin\alpha_0 \tag{21}$$

By minimizing the total energy density $\epsilon_{tot}(\theta_0, \alpha_0)$ with respect to its arguments, in the absence of in-plane anisotropies one thus obtains the equilibrium value for the stripe

rotation angle to be $\alpha_0^{eq} = 90^\circ$ for any value of H^x. Whereas, the equilibrium out-of-plane maximum canting angle, θ_0^{eq}, does depend on the in-plane applied field intensity, H^x.

In figure 12, the contour plots of $\epsilon_{tot}(\theta_0, \alpha_0)$ are reported for selected values of H^x, ranging from 100 Oe to 1750 Oe. Note that the latter value turns out to be the in-plane saturation field H_s for $K_{PMA} = 6.3 \times 10^6$ erg/cm^3. As it can be seen, the total energy density $\epsilon_{tot}(\theta_0, \alpha_0)$ has only one minimum, corresponding to the configuration III in figure 10, with $\alpha_0^{eq} = 90^\circ$. On increasing H^x, α_0^{eq} remains constant, while θ_0^{eq} decreases. At the saturation field H_s= 1750 Oe, the out-of-plane maximum canting angle vanishes ($\theta_0^{eq} \to 0$), and the magnetization lies entirely in the film plane ($m = M_{IP}/M_s = (\sin\theta_0^{eq})/\theta_0^{eq} \to 1$). Note that for any value of $H^x > 0$, the minimum of $\epsilon_{tot}^{III}(\theta_0, \alpha_0)$ is deeper than both minima of $\epsilon_{tot}^{I}(\theta_0, \varphi_0)$ and $\epsilon_{tot}^{II}(\theta_0, \varphi_0)$ (cfr. figure 13(d) later on).

The dependence of the total energy density of the three configurations as a function of the transversal field intensity H^x can be used to explain the existence of a threshold field for the reorientation of the stripes axis. However, it is important to note that, for field intensities where different metastable states are possible, the configuration assumed by the system can not be predicted only on the basis of energetic considerations, but also the history of the sample must be taken into account. We observe that, in the low field range (200-380 Oe) where the three configurations are locally (I and II) or globally (III) stable, the configuration I (red symbols) and the configuration III (blue symbols) have similar values of the out-of-plane maximum canting angle θ_0^{eq} (figure 13(b)), and thus similar values of the in-plane magnetization (figure 13(c)). In contrast, the configuration II (grey symbols) has a sensibly lower value of θ_0^{eq} (figure 13(a)) and consequently an almost saturated in-plane magnetization ($m \gtrsim 0.9$ in figure 13(c)). Starting from remanence with the stripes aligned along the y axis, the system is allowed to remain in the configuration I even when the intensity of the transversal field H^x is increased, as far as this configuration remains locally stable. On further increasing H^x, a jump to the configuration III is expected to occur when the configuration I becomes unstable: i.e., at $H_{trans}^{thr} = 380$ Oe. The reorientation of the stripes axis towards the field direction is associated with a large rotation angle ($\alpha_0^{eq} = 90^\circ$ in figure 13(b)). In contrast, the out-of-plane maximum canting angle θ_0^{eq} has a small (though finite) variation, see figure 13(b). Note that, passing from I to III at H_{trans}^{thr}, a noticeable lowering of the energy is realized, as it can be seen in figure 13(d). In Appendix B, the various contributions to the total energy density ϵ_{tot} were calculated versus H^x. From figure B1(a-c) it appears that the decrease of the equilibrium out-of-plane maximum canting angle θ_0^{eq} on increasing H^x determines the increase of the PMA contribution ϵ_K, and the decrease of all the other contributions (in particular the transversal field contribution $\epsilon_{H,trans}$, and the surface magnetostatic contribution ϵ_S). In order to minimize the cost in PMA energy, it is then energetically preferred for the system to undergo a small variation of the out-of-plane maximum canting angle θ_0^{eq} at H_{trans}^{thr} accompanied by a large in-plane rotation ($\alpha_0^{eq} = 90^\circ$) of the stripes axis (see figure 13(b)), rather than a large variation of

θ_0^{eq} without stripe rotation (see figure 13(a)). Namely, the configuration II is expected not to be realized, in spite of its being locally stable and lower in energy than I in the low field range (H^x =200-380 Oe, see figure 13(d)).

In order to better understand the dependence of H_{trans}^{thr} on the intensity of the perpendicular magnetic anisotropy, we have determined the equilibrium configurations of the system in a transversal magnetic field, H^x, using different values of K_{PMA} in the range from 5.5 to 6.3×10^6 erg/cm^3. (Note that within the 1D model of stripe domains [19], an upper limit to K_{PMA} is imposed by the condition $\theta_0^{eq} \leq 90°$.) In figure 14(a-c), the calculated out-of-plane maximum canting angle θ_0^{eq} is shown versus H^x (below and above H_{trans}^{thr}, red and blue symbols, respectively) for three increasing values of the out-of-plane uniaxial anisotropy K_{PMA}. As it can be seen, the higher K_{PMA}, the further the configuration I remains stable, and as a consequence the higher is the reorientation threshold field H_{trans}^{thr}, marked by a vertical dashed line in Fig. 14. Similarly, the higher K_{PMA}, the higher is the in-plane saturation field H_s, marked by a vertical short-dash-dotted line in figure 14.

In figure 15, the calculated threshold field for stripe reorientation, H_{trans}^{thr}, and in-plane saturation field, H_s, are reported versus the intensity of the perpendicular magnetic anisotropy. For both quantities, a linear dependence is obtained in the investigated range of K_{PMA}, although with a different slope. (A third quantity reported in figure 15, also showing a linear dependence on K_{PMA}, is the rotatable anisotropy field, $H_{rot,0}$, discussed later on in section 5.) These results are in qualitative agreement with experimental data obtained for both Fe-N (figure 7(a)) and $Fe_{78}Si_9B_{13}$ [42] films. Clearly, in order to obtain a quantitative estimate of the reorientation threshold field intensity H_{trans}^{thr} for a given film system, one should definitely resort to a more realistic 2D model of the stripe domains. A 2D model with closure stripe domains should be required (as it was proved in the very similar case of a Fe-Ga film [38]) to account also for other subtle features, such as the linear dependence of M_{ON}/M_s on H_{reor}^{thr} experimentally observed (figure 6(a)) in our Fe-N samples. Nevertheless, the 1D model [19] is valuable since it provides a straightforward explanation of the linear dependence of H_{trans}^{thr} and H_s on the PMA in terms of the equilibrium out-of-plane maximum canting angle θ_0^{eq}, which would hardly be obtained by numerical methods and/or more refined theoretical models.

5. The rotatable anisotropy in Fe-N films with weak stripe domains

A further advantage of the 1D model [19] is that it allowes us to theoretically investigate another peculiar property of weak stripe domains, the so-called "rotatable" anisotropy, which consists in the possibility of selecting the easy magnetization direction in the film plane simply by applying a sufficiently large magnetic field along this direction [76, 77, 20, 78]. The rotatable anisotropy strongly affects the magneto-dynamic properties of the thin films [79, 37] since it provides an energy barrier which prevents the free in-plane rotation of the magnetization vector. As a matter of fact, the rotatable

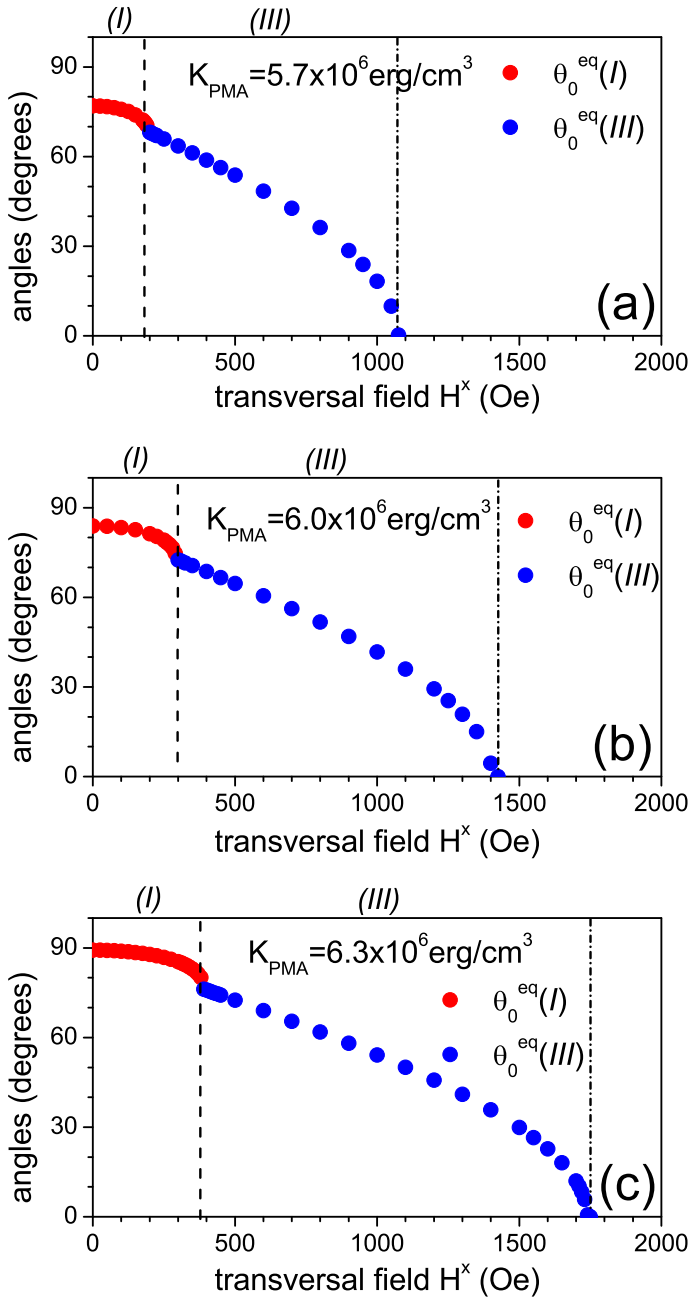

Figure 14. (Color online) The equilibrium out-of-plane maximum canting angle θ_0^{eq} calculated versus the intensity of a transversal magnetic field, H^x. Panels (a), (b), and (c) refer to three increasing values of the perpendicular magnetic anisotropy, K_{PMA}. The vertical dashed line denotes the position of the reorientation threshold field, H_{trans}^{thr}, at which the stripe pattern rotates abruptly, passing from configuration I to III. The vertical short-dash-dotted line denotes the position of the saturation field, H_s.

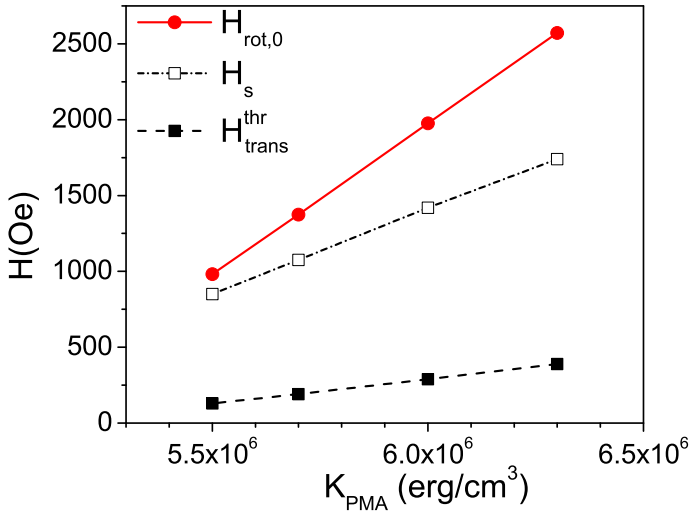

Figure 15. (Color online) Black squares: The reorientation threshold field, H^{thr}_{trans}, versus the intensity of the perpendicular magnetic anisotropy, K_{PMA}. Open squares: The saturation field, H_s, versus K_{PMA}. Red circles: The rotatable anisotropy field calculated at remanence, $H_{rot,0}$, versus K_{PMA}. The lines are guides to the eye.

anisotropy has been termed as a pseudo-uniaxial in-plane anisotropy [20] because its magnitude is not constant, but depends on the intensity of the applied magnetic field [79, 37].

Using the equilibrium values for the angles θ_0 and φ_0, we calculated the rotatable anisotropy field H_{rot}, as given by equation (14), for three different values of K_{PMA} (the same as in figure 14). H_{rot} is reported in figure 16 versus the intensity of an applied magnetic field, either transversal (H^x, red circles) or longitudinal (H^y, black line) to the stripes axis. One can see that H_{rot} assumes the maximum value for H^x=0. On increasing the applied field intensity H^x, the rotatable anisotropy field H_{rot} starts to decrease because the angle θ_0^{eq} decreases (namely, the in-plane magnetization increases), up to vanish when the stripe pattern disappears for $\theta_0 = 0$ (namely, the in-plane magnetization becomes saturated). In addition, H_{rot} versus H^x exhibits a discontinuity at the threshold field H^{thr}_{trans}, which becomes more marked on increasing K_{PMA}. Above the reorientation threshold field, there is no difference between the value of the rotatable anisotropy field calculated for transversal or longitudinal field. In fact, in the configuration III the stripes have rigidly rotated by an angle $\alpha_0 = 90°$, and therefore, the stripes axis has become parallel to the direction of the applied field.

Note that, in the longitudinal field configuration, our calculations within the 1D model [19] predict a quasi-linear decrease of H_{rot} (see figure 16) versus the applied field intensity, H^y, in qualitative agreement with recent experimental findings in thin films with weak stripe domains: e.g., permalloy films investigated by ferromagnetic resonance (FMR, cfr. figure 2(b) in [79] and figure 4 in [80]), and Fe-Ga films investigated by Brillouin light scattering (BLS, cfr. figure 4 in [37]). Moreover, from figure 16 it

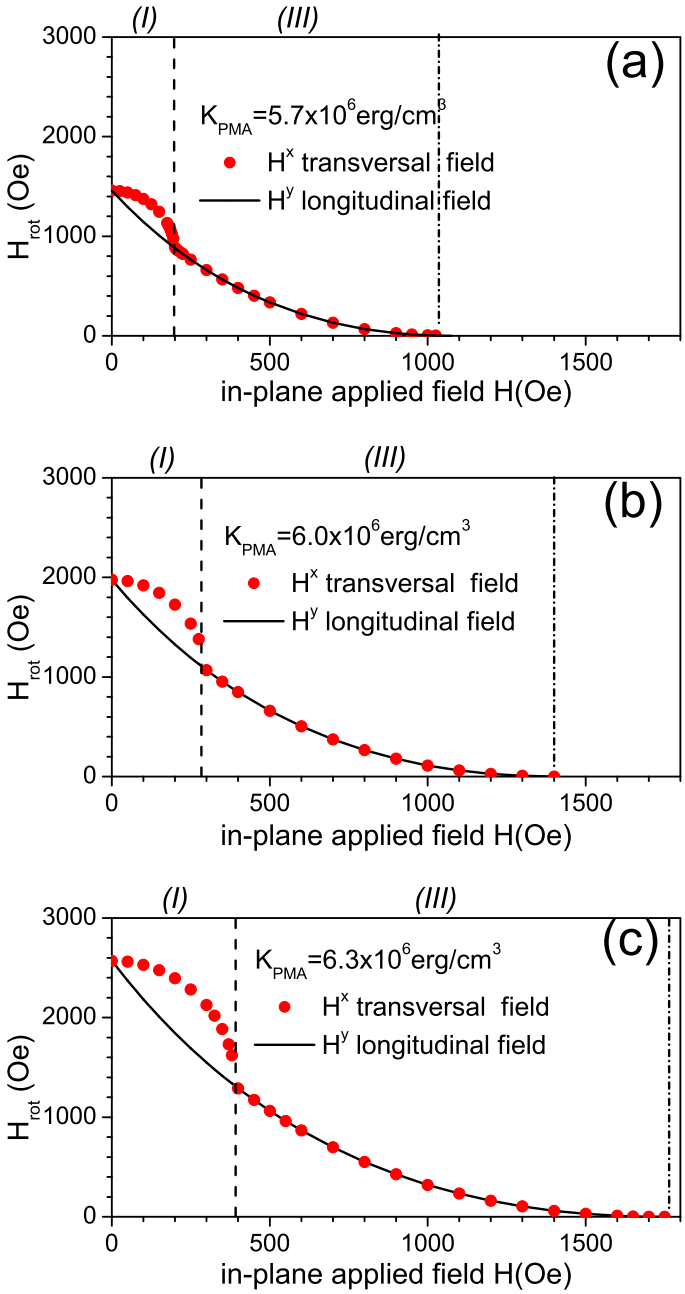

Figure 16. (Color online) The rotatable anisotropy field, H_{rot}, versus the intensity of an in-plane magnetic field, applied either in the transversal direction (H^x, red points) or in the longitudinal one (H^y, black line) with respect to the stripes axis. The calculation was performed for three different values of K_{PMA}, the same as in figure 14.

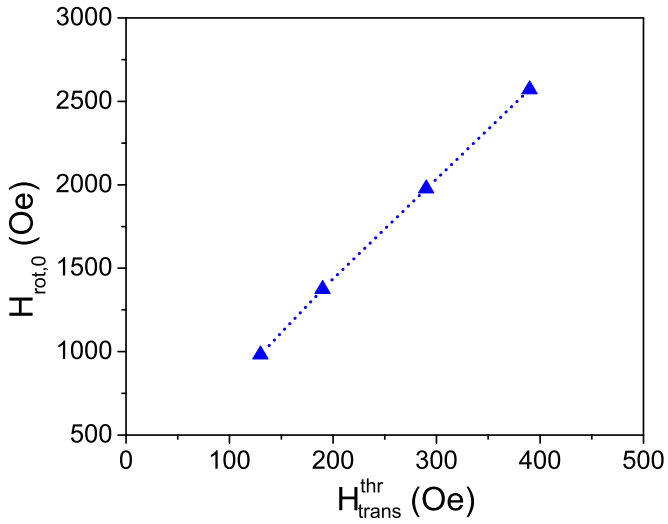

Figure 17. (Color online) The rotatable anisotropy field at remanence $H_{rot,0}$ versus the reorientation threshold field H_{trans}^{thr}, calculated for different values of K_{PMA}, ranging from 5.5 to 6.3×10^6 erg/cm^3 (cfr. figure 15).

appears that the rotatable anisotropy field at remanence increases on increasing the perpendicular magnetic anisotropy. In particular, using equation (14) we have calculated $H_{rot,0}$ and found a linear dependence on K_{PMA}, as shown in figure 15 (red circles). Such a feature turns out to be in qualitative agreement with a recent experimental study [93] in ferrite doped FeNi thin films, where an increase of the rotatable anisotropy field H_{rot} on increasing the perpendicular magnetic anisotropy was observed by FMR measurements.

Finally, we have found that a linear correlation holds, see figure 17, between the rotatable anisotropy field at remanence, $H_{rot,0}$, and the reorientation threshold field, H_{trans}^{thr}. This finding indicates that, although the rotatable anisotropy field (namely, the field proportional to the energy barrier preventing from the free in-plane rotation of the magnetization vector) and the threshold field (namely, the transversal field to be overcome in order to induce the reorientation of stripe domains) are in principle distinct, they are both driven by the PMA, which is responsible for the onset of the weak stripe domains.

6. Conclusions

In this work, the reorientation of weak stripe domains, driven by a transversal magnetic field greater than a threshold value, has been investigated in Fe-N thin films both experimentally and theoretically. The samples have been prepared by ion implantation of nitrogen molecular ions N_2^+ on an α-Fe film, epitaxially grown on ZnSe/GaAs(001). We found that the PMA strength of the Fe-N films can be tuned on changing both ion implantation and heat treatment conditions. MFM images disclosed very regular stripe domains which at remanence are aligned along the last saturation direction. Applying a

magnetic field H_{trans} perpendicular to the stripe axis and having an increasing intensity, the stripe domains reorientation has been observed when H_{trans} is larger than a threshold field H_{trans}^{thr}. Interestingly, a linear increase of the H_{trans}^{thr} value on increasing the PMA strength has been observed by VSM measurements. This linear behaviour of H_{trans}^{thr} has been interpreted by using a one-dimensional model of the weak stripe domains, which allowed us to calculate the different terms in the total energy density. Various possible equilibrium magnetization congurations have been considered, depending on the intensity of the magnetic field applied perpendicularly to the stripe domain axis. The maximum canting angle of the stripe domain magnetization out of the film plane has been shown to be the essential parameter to explain the linear dependence of both H_{trans}^{thr} and $H_{rot,0}$ as a function of the PMA. In addition, the effective rotatable anisotropy field at remanence, $H_{rot,0}$, was also found to linearly increase with the PMA intensity. These findings indicate that both H_{trans}^{thr} and $H_{rot,0}$ are driven by the PMA, although these two quantities affect different magnetic properties of the stripes domains, i.e. the static and dynamic magnetic behavior, respectively. We expect that the present work will provide the basis for a better understanding of the reorientation mechanism of stripe magnetic domains, paving the way to the possible exploitation of stripe patterns to guide and control the propagation of spin waves, or spin textures such as bubbles and skyrmions, in thin magnetic films.

Acknowledgments

We thank F. Fortuna for ion implantation performed at CSNSM Université Paris Sud-CNRS, Paola Atkinson for the MBE growth of buffer layers of GaAs at INSP and the staff of the MPBT (physical properties-low temperature) platform of Sorbonne University for their support. M. Coïsson at INRIM is gratefully acknowledged for fruitful discussions on the threshold field for the reorientation of the stripe domain pattern in FeSiB films, as well as for sending us a preprint of his paper on the subject [42].

Appendix A. Wide-wall and narrow-wall 1D models for weak and strong stripe domains

In this appendix, we compare a few, paradigmatic 1D models which have been proposed in the literature to describe stripe domain patterns in magnetic films. At the same time, we suggest a harmonization of the nomenclature according to the shape of the periodic wave $\theta(x)$, where θ is the out-of-plane canting angle of the magnetization and x is the in-plane direction perpendicular to the stripes axis (see figure 8).

A first distinction has to be made between wide-wall and narrow-wall models, depending on the ratio between the wall width, δ, and the stripe width, d. In a ferromagnetic film with exchange A_{ex} per unit length and a perpendicular anisotropy energy density K_{PMA}, an estimate for the wall width is $\delta = \pi \sqrt{A_{ex}/K_{PMA}}$ [6]. The wall width can be rewritten as $\delta = \pi l_{ex}/\sqrt{Q}$, in terms of the quality factor

$Q = K_{PMA}/K_d$ (where $K_d = 2\pi M_s^2$ is the magnetostatic energy density), and of the exchange length $l_{ex} = \sqrt{A_{ex}/K_d}$. Hence, it follows that films with a weak PMA (low Q) will have wide domain walls, while films with a strong PMA (high Q) will have narrow domain walls. For a given 1D angle profile, $\theta(x)$, with period $P = 2d$, see figure A1, we adopt the following definition of the wall width [94]

$$\delta = \frac{2\theta_0}{\theta_0'} \tag{A.1}$$

where θ_0 is the maximum of $\theta(x)$ at the middle of the magnetic domain (i.e., for $x = d/2$ in figure A1), and θ_0' is the slope of $\theta(x)$ at the middle of the wall (i.e., for $x = 0$ in fugure A1).

The 1D profile we have chosen in this work for the out-of-plane canting angle $\theta(x)$ (see equation (2) and figure 8(c)) is the 1D triangular-wave angle profile originally proposed by Saito *et al.* [19] for Permalloy films with a weak PMA. We note that the term "triangular-wave" appears to be more appropriate than the "sawtooth-wave" one frequently used in the literature [20, 22, 80]. Indeed, the triangular wave is the absolute value of the sawtooth wave [95]. The triangular-wave profile is reported in panel (a1) (black line), and represents an extreme case of a wide-wall model because the wall width is just equal to the domain width: $\delta = d$. The corresponding out-of-plane magnetization profile, $M^z(x) = M_s \sin\theta(x)$, is reported in panel (b1).

In contrast, a 1D square-wave profile for $\theta(x)$ was originally proposed by Kittel [96] for films with a strong PMA. The square-wave angle profile is reported in panel (a2)(blue line), and it generates a square-wave profile also for the magnetization $M(x)$, see panel (b2). The square-wave profile represents an extreme case of a narrow-wall model because the wall width is exactly zero: $\delta = 0$.

Later on, other 1D models of stripe magnetic domains have been proposed, which allow one to consider the intermediate case $0 < \delta < d$. Alvarez-Prado *et al.* [20] suggested a 1D sine-wave angle profile, $\theta(x) = \theta_0 \sin(\pi x/d)$, with period $2d$ as shown in panel (a1) (red line). The corresponding out-of-plane magnetization profile, $M^z(x) = M_s \sin\theta(x)$, is reported in panel (b1). Using the definition (A.1), one obtains $\delta = (\frac{2}{\pi})d$, namely a wide-wall model of the stripe domains, which is expected to provide good results in films with weak stripe domains, i.e. for $Q < 0.5$.

In contrast, Virot *et al.* [22] and subsequently Wei *et al.* [80] suggested a 1D trapezoidal-wave profile for $\theta(x)$, reported in panel (a2). The only difference between the two authors is the fact that Virot *et al.* imposed the maximum out-of-plane canting angle to be $\theta_0 = \pi/2$, while Wei *et al.* allowed for $\theta_0 < \pi/2$. Virot *et al.* showed that the trapezoidal-wave profile is especially well suited for films with strong stripe domains, i.e. for $0.5 < Q < 1.0$, and it can be applied even to the case $Q > 1$. Thus, the trapezoidal-wave profile can be considered as a narrow-wall model. As a matter of fact, a recent analysis [94] of the in-plane magnetization curves in 70-nm-thick Fe-Ga films with weak stripe domains ($Q = 0.3$) confirmed that a 1D trapezoidal-wave angle profile provides a less consistent description of the experimental data than a sine-wave profile.

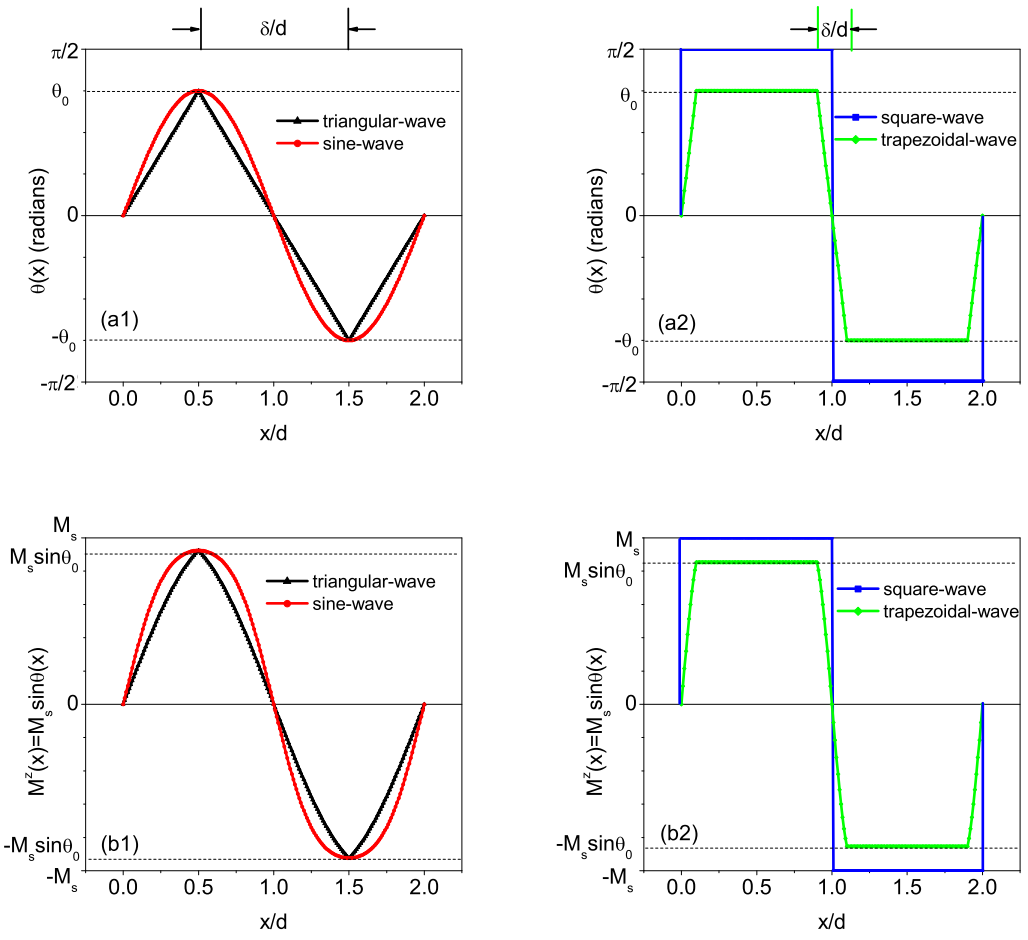

Figure A1. (Color online) Comparison between some paradigmatic wide-wall (a1,b1) and narrow-wall (a2,b2) 1D models, for weak and strong stripe domains respectively. The profiles of the out-of-plane canting angle, $\theta(x)$ are shown in (a1) and (a2); the corresponding profiles of the out-of-plane magnetization component, $M^z(x) = M_s \sin \theta(x)$, in (b1) and (b2). The arrows on top of panels (a1) and (a2) point the wall width (δ, in units ot the domain width, d), respectively for a wide-wall ($\delta = d$) triangular-wave profile [19] and a narrow-wall ($\delta \ll d$) trapezoidal-wave profile [22, 80]. The sine-wave profile [20] in (a1) has $\delta = \frac{2}{\pi} d$ (not shown), while the square-wave profile [96] in (a2) has $\delta = 0$.

In the present article, our main aim is to investigate the reorientation of weak stripe magnetic domains when a dc magnetic field is applied in plane perpendicularly to the stripes axis, with intensity H_{trans} greater than a threshold value. Our Fe-N thin films are characterized by a quality factor Q comprised in the range between 0.28 and 0.38, depending on the preparation conditions. Therefore, our films are in the weak-stripe regime, and a wide-wall model is expected to provide better results than a narrow-wall model. Our adoption of the simplest wide-wall model, i.e. the 1D triangular-wave angle profile [19] in equation (2), is motivated by the fact that it allows

us to obtain approximate expressions for the magnetic energy density contributions in the transparent, analytic form of equations (4), (5), (11), (12), and (18a). In this way, understanding the role of the model parameters in the stripe domains reorientation induced by a transversal magnetic field turns out to be easier than using any other periodic wide-wall waveform. Furthermore, we do not expect that using more sophisticated 1D models would lead to substantial improvements in the theoretical interpretation of the stripe reorientation mechanism.

Appendix B. Energy density contributions in a transversal magnetic field

In this appendix, we show the calculated equilibrium configurations and magnetic energy density of the magnetic film versus the the intensity (H^x) of a transversal field: i.e., a magnetic field applied in plane perpendicular to y, the direction of the stripes axis at remanence.

In figure B1(a), the equilibrium angles calculated using the same Hamiltonian parameters as in figure 13(b), have been reported for $0 < H^x < H^{thr}_{trans}$ and $H^{thr}_{trans} < H^x < H_s$ (configurations I and III, respectively).

In figure B1(b), the total magnetic energy density $\epsilon_{tot} = \epsilon_A + \epsilon_K + \epsilon_S + \epsilon_V + \epsilon_{H,trans}$, calculated as a function of the transversal field intensity, H^x, has been separated into its various contributions. We report $\epsilon_{tot}(\theta^{eq}_0, \varphi^{eq}_0)$ for $0 < H^x < H^{thr}_{trans}$, and $\epsilon_{tot}(\theta^{eq}_0, \alpha^{eq}_0)$ for $H^{thr}_{trans} < H^x < H_s$, respectively. The various contributions are: ϵ_A, from exchange coupling; ϵ_K, from PMA anisotropy; ϵ_S and ϵ_V, from surface and volume magnetic dipole-dipole interactions, respectively; $\epsilon_{H,trans}$, from the Zeeman energy associated with the transversal magnetic field. Their explicit expressions are given by Eqs. 4, 5, 11, 12, and 18*a*, respectively.

One observes that the contributions ϵ_A, ϵ_S, and $\epsilon_{H,trans}$ are decreasing functions of H^x, and that only the uniaxial anisotropy contribution ϵ_K is an increasing function of the transversal field intensity in the whole field range $0 < H^x < H_s$. Moreover, note that the increase of the uniaxial anisotropy contribution ϵ_K is associated (see Eq. 5) with the decrease of the out-of-plane maximum canting angle θ^{eq}_0. At the saturation field H_s, when the magnetization lies entirely within the film plane, one has $\theta^{eq}_0 = 0$ and $\epsilon_K = 0$. Also the volume dipolar contribution ϵ_V is an increasing function of H^x, but it is nonzero only in the range $0 < H^x < H^{thr}_{trans}$ (see figure B1(c)): i.e., when the equilibrium in-plane uniform canting angle φ_0 is nonzero (cfr. Eq. 12). At the reorientation threshold field H^{thr}_{trans}, all contributions undergo a discontinuity as a consequence of the step in the equilibrium out-of-plane maximum canting angle θ^{eq}_0 on passing from the configuration I to the configuration III.

Summing up, as a result of all contributions, the total energy density ϵ_{tot} (open circles in figure B1(b)) is found to decrease discontinuously on increasing the intensity, H^x, of the transversal magnetic field.

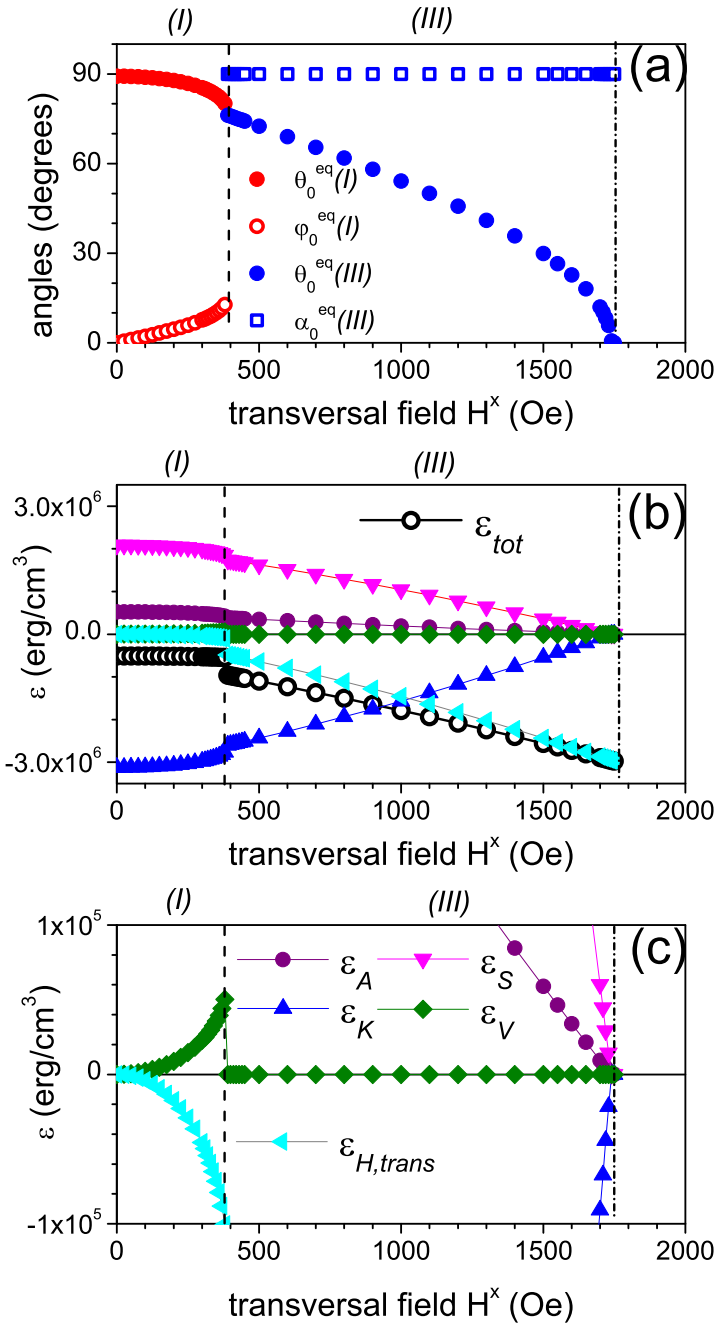

Figure B1. (Color online) The calculated configurations and magnetic energy density of the film versus the intensity, H^x, of a magnetic field transversal to the stripes axis. (a): The equilibrium angles (θ_0, φ_0) for the configuration I, and (θ_0, α_0) for the configuration III, respectively. (b) and (c): The total magnetic energy density, ϵ_{tot}, and its various contributions (see text). Please note that (c) is a zoom of (b) around $\epsilon = 0$.

Appendix C. Energy density contributions in a longitudinal magnetic field

For the sake of completeness, we have also calculated the equilibrium configuration and magnetic energy density of the magnetic film versus the the intensity (H^y) of a longitudinal field: i.e., a magnetic field applied in plane parallel to y, the direction of the stripes axis at remanence. In such a geometry, the angle φ_0 in figure 8(a) vanishes for symmetry reasons in the whole field range: $\varphi_0 = 0$ for $0 < H^y < H_s$. Therefore, the total energy density $\epsilon_{tot}(\theta_0, \varphi_0 = 0) = \epsilon_A + \epsilon_K + \epsilon_S + \epsilon_V + \epsilon_{H,long}$ has to be minimized solely with respect to the variable θ_0. The various terms in the summation are respectively given by Eqs. 4, 5, 11, 12, and 18*b*.

For increasing values of the longitudinal field intensity, a monotonic and continuous decrease of θ_0^{eq} is found in the whole field range $0 < H^y < H_s$, as displayed in figure C1(a). Therefore, the normalized in-plane magnetization, $m = M_{IP}/M_s = (\sin\theta_0^{eq})/\theta_0^{eq}$, is found to increase in a monotonic and continuous way in the same range, see figure C1(b). In figure C1(c), the calculated total magnetic energy density $\epsilon_{tot}(\theta_0^{eq}, \varphi_0^{eq})$ is reported versus H^y, separated into its various contributions. One observes that ϵ_A, ϵ_S, and $\epsilon_{H,long}$ are decreasing functions of H^y (see Eqs. 4, 11 and 18*b*). The dipolar volume contribution is $\epsilon_V = 0$ in the whole field range $0 < H^y < H_s$ because by symmetry one has $\varphi_0^{eq} = 0$ (see Eq. 12). Only the uniaxial anisotropy contribution ϵ_K is a monotonic and continuous increasing function of H^y ($\epsilon_K \to 0$ for $\theta_0^{eq} \to 0$, see Eq. 5).

Summing up, as a result of all contributions, the total energy density ϵ_{tot} (open circles in figure C1(c)) is found to decrease in a monotonic and continuous way on increasing the intensity, H^y, of the longitudinal magnetic field.

ORCID iDs

https://orcid.org/

Louis-Charles Garnier 0000-0003-3658-3263
Massimiliano Marangolo 0000-0001-6211-8168
Mahmoud Eddrief 0000-0002-4822-2185
Diego Bisero 0000-0003-2610-6519
Samuele Fin 0000-0002-8971-2463
Francesca Casoli 0000-0002-4323-0362
Maria Gloria Pini 0000-0002-6571-4181
Angelo Rettori 0000-0002-4311-234X
Silvia Tacchi: 0000-0003-1403-2268

References

[1] Seul M and Andelman D 1995 *Science* **267** 476
[2] Emery V J, Kivelson S A and Tranquada J M 1999 *Proc. Natl. Acad. Sci. USA* **96** 8814
[3] Keller S L and Mc Connell H M 1999 *Phys. Rev. Lett.* **82** 1602

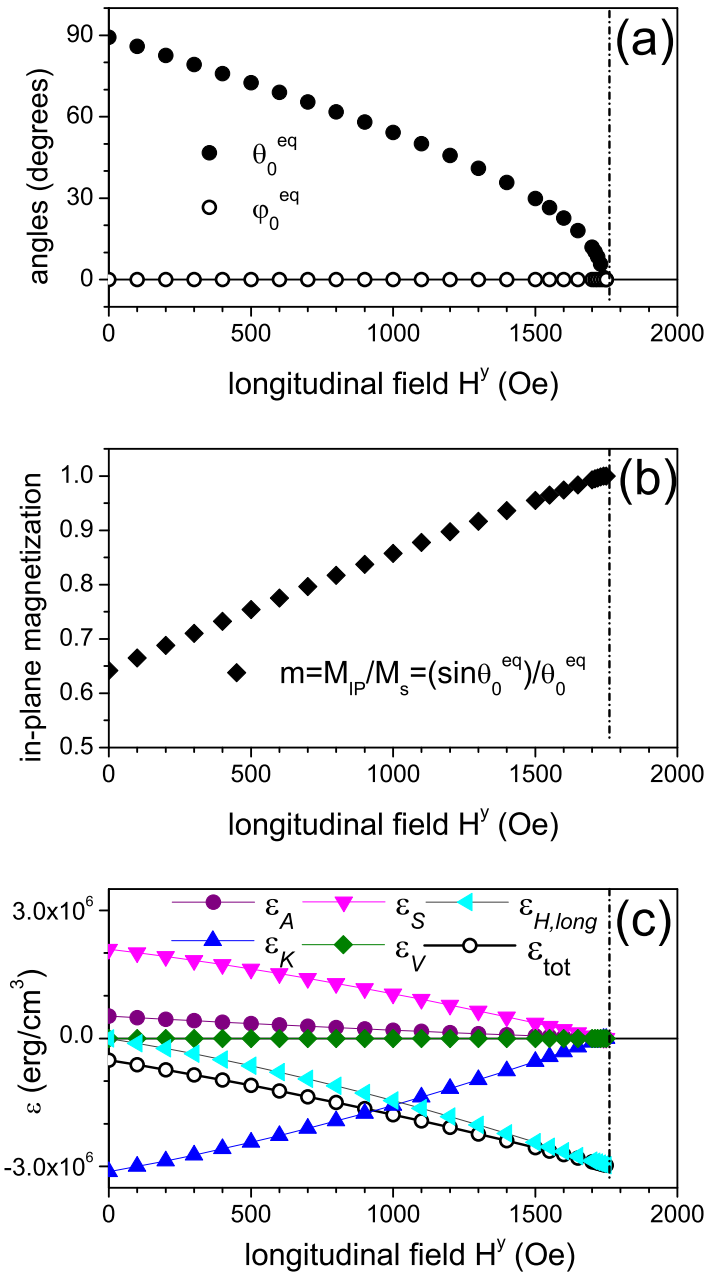

Figure C1. (Color online) The calculated configuration and magnetic energy density of the film versus the intensity, H^y, of a longitudinal magnetic field (i.e. applied in plane parallel to the stripes axis). (a) The equilibrium angles (θ_0, φ_0). For symmetry reason, one has $\varphi_0^{eq} = 0\ \forall H^y$. (b) (c) The total energy density ϵ_{tot}, and its various contributions (see text).

[4] Saratz N, Lichtenberger A, Portmann O, Ramsperger U, Vindigni A and Pescia D 2010 *Phys. Rev. Lett.* **104** 077203
[5] Cinti F and Boninsegni M 2019 *J. Low Temp. Phys.* **196** 413
[6] Hubert A and Schäfer R 1998 *Magnetic Domains: The Analysis of Magnetic Microstructures* (Berlin: Springer)
[7] Kittel C 1949 *Rev. Mod. Phys.* **21** 541–583
[8] Kooy C and Enz U 1960 *Philips Res. Repts* **15** 7–29
[9] Cape J A and Lehman G W 1971 *Journal of Applied Physics* **42** 5732–5756
[10] Druyvesteyn W F and Dorleijn J W F 1971 *Philips Res. Repts.* **26** 11–28
[11] Hubert A 1975 *J Appl Phys* **46** 2276–2287
[12] Allenspach R, Stampanoni M and Bischof A 1990 *Phys. Rev. Lett.* **65** 3344–3347
[13] Barnes J R, OShea S J, Welland M E, Kim J Y, Evetts J E and Somekh R E 1994 *J Appl Phys* **76** 2974–2980
[14] Davies J E, Hellwig O, Fullerton E E, Denbeaux G, Kortright J B and Liu K 2004 *Phys Rev B* **70** 227
[15] Thiele J U, Folks L, Toney M F and Weller D K 1998 *Journal of Applied Physics* **84** 5686–5692
[16] Draaisma H J G and de Jonge W J M 1987 *J Appl Phys* **62** 3318–3322
[17] Kaplan B and Gehring G A 1993 *J. Magn. Magn. Mater.* **128** 111–116
[18] Murayama Y 1966 *J. Phys. Soc. Jpn.* **21** 2253–2266
[19] Saito N, Fujiwara H and Sugita Y 1964 *J. Phys. Soc. Jpn.* **19** 1116–1125
[20] Álvarez-Prado L M, Pérez G T, Morales R, Salas F H and Alameda J M 1997 *Phys. Rev. B* **56** 3306–3316
[21] Kisielewski M, Maziewski A, Polyakova T and Zablotskii V 2004 *Phys Rev B* **69** 6966
[22] Virot F, Favre L, Hayn R and Kuzmin M D 2012 *J. Phys. D: Appl. Phys.* **45** 405003
[23] Luo F, Zheng F, Yin G, Wu D and Wei F 2013 *Appl. Phys. Express* **6** 073003
[24] Lemesh I, Büttner F and Beach G S D 2017 *Phys Rev B* **95** 7
[25] Palatnik L S, Pavlik A G and Samofalov V N 1977 *Fiz. Tverd. Tela* **19** 830–836
[26] Naik R, Heemed S, Talagala P and Wenger L E 2002 *J. Appl. Phys.* **91** 7550–7552
[27] la Brune M and Miltat J 1994 *J. Appl. Phys.* **75** 21562168
[28] Fallarino L, O H and A B 2016 *Phys Rev B* **94** 064408
[29] Dubovik M N and Filippov B N 2017 *Physics of Metals and Metallography* **118** 1031–1039
[30] Singh S, Gao H and Hartmann U 2018 *Phys. Rev. B* **98** 060414
[31] Fin S, Silvani R, Tacchi S, Marangolo M, Garnier L-C, Eddrief M, Hepburn C, Fortuna F, Rettori A, Pini M G and Bisero D 2018 *Sci. Rep.* **8** 9339
[32] Muller M 1961 *Phys Rev* **122** 1485–1489
[33] Brown W 1961 *Phys Rev* **124** 1348–1353
[34] Spain R J 1963 *Appl Phys Lett* **3** 208–209
[35] Resnick D A, McClure A, Kuster C M, Rugheimer P and Idzerda Y U 2011 *J Appl Phys* **109** 07A938
[36] Barturen M, Rache Salles B, Schio P, Milano J, Butera A, Bustingorry S, Ramos C, de Oliveira A J A, Eddrief M, Lacaze E, Gendron F, Etgens V H and Marangolo M 2012 *Appl Phys Lett* **101** 092404
[37] Tacchi S, Fin S, Carlotti G, Gubbiotti G, Madami M, Barturen M, Marangolo M, Eddrief M, Bisero D, Rettori A and Pini M G 2014 *Phys. Rev. B* **89** 024411
[38] Fin S, Tomasello R, Bisero D, Marangolo M, Sacchi M, Popescu H, Eddrief M, Hepburn C, Finocchio G, Carpentieri M, Rettori A, Pini M G and Tacchi S 2015 *Phys. Rev. B* **92** 224411
[39] Garnier L-C, Eddrief M, Fin S, Bisero D, Fortuna F, Etgens V H and Marangolo M 2016 *SPIN* **6** 1640014
[40] Camara I S, Tacchi S, Garnier L-C, Eddrief M, Fortuna F, Carlotti G and Marangolo M 2017 *J. Phys.: Condens. Matter* **29** 465803
[41] Coïsson M, Celegato F, Olivetti E, Tiberto P, Vinai F and Baricco M 2008 *J Appl Phys* **104**

033902
[42] Coïsson M, Barrera G, Celegato F and Tiberto P 2019 *Appl. Surf. Sci* **476** 402–411
[43] Yamanouchi M, Jander A, Dhagat P, Ikeda S, Matsukura F and Ohno H 2011 *IEEE Magn. Lett.* **2** 3000304–3000304
[44] Viala B, Minor M K and Barnard J A 1996 *J Appl Phys* **80** 3941–3956
[45] Miguel J, Peters J F, Toulemonde O M, Dhesi S S, Brookes N B and Goedkoop J B 2006 *Phys Rev B* **74** 953
[46] Hierro-Rodriguez A, Vélez M, Morales R, Soriano N, Rodríguez-Rodríguez G, Álvarez-Prado L M, Martín J I and Alameda J M 2013 *Phys. Rev. B* **88** 174411
[47] Kotani A, Nakajima H, Harada K, Ishii Y and Mori S 2016 *Phys Rev B* **94** 024407
[48] Labrune M and Thiaville A 2001 *Eur. Phys. J. B* **23** 17–28
[49] Bručas R, Hafermann H, Katsnelson M I, Soroka I L, Eriksson O and Hjörvarsson B 2004 *Phys Rev B* **69** 178
[50] Fallarino L, Oelschlägel A, Arregi J A, Bashkatov A, Samad F, Böhm B, Chesnel K and Hellwig O 2019 *Phys. Rev. B* **99** 024431
[51] Markó D, Valdés-Bango F, Quirós C, Hierro-Rodriíguez A, Vélez M, Martín J I, Alameda J M, Schmool D S and Álvarez-Prado L M 2019 *Appl. Phys. Lett.* **115** 082401
[52] Sander D, Valenzuela S O, Makarov D, Marrows C H, Fullerton E E, Fischer P, McCord J, Vavassori P, Mangin S, Pirro P, Hillebrands B, Kent A D, Jungwirth T, Gutfleisch O, Kim C G and Berger A 2017 *J. Phys. D: Appl. Phys.* **50** 363001
[53] Lee J C T, Chess J J, Montoya S A, Shi X, Tamura N, Mishra S K, Fischer P, McMorran B J, Sinha S K, Fullerton E E, Kevan S D and Roy S 2016 *Appl Phys Lett* **109** 022402
[54] Nakajima H, Kawase H, Kurushima K, Kotani A, Kimura T and Mori S 2017 *Phys Rev B* **96** 024431
[55] Montoya S A, Couture S, Chess J J, Lee J C T, Kent N, Henze D, Sinha S K, Im M Y, Kevan S D, Fischer P, McMorran B J, Lomakin V, Roy S and Fullerton E E 2017 *Phys Rev B* **95** 7
[56] Peng L, Zhang Y, He M, Ding B, Wang W, Tian H, Li J, Wang S, Cai J, Wu G, Liu J P, Kramer M J and Shen B g 2017 *npj Quantum Materials* **2** 30
[57] Ruth M E, Iacocca E, Kevrekidis P G and Hoefer M A 2018 *Phys Rev B* **97** 104428
[58] Parkin S and Yang S H 2015 *Nature Nanotechnology* **10** 195
[59] Jiang W, Upadhyaya P, Zhang W, Yu G, Jungfleisch M B, Fradin F Y, Pearson J E, Tserkovnyak Y, Wang K L, Heinonen O, te Velthuis S G E and Hoffmann A 2015 *Science* **349** 283
[60] Weiss R, Mattheis R and Reiss G 2013 *Meas. Sci. Technol.* **24** 082001
[61] Fert A, Reyren N and Cros V 2017 *Nature Reviews Materials* **2** 17031
[62] Miron I M, Moore T, Szambolics H, Buda-Prejbeanu L D, Auffret S, Rodmacq B, Pizzini S, Vogel J, Bonfim M, Schuhl A and Gaudin G 2011 *Nature Materials* **10** 419
[63] Lemesh I, Litzius K, Böttcher M, Bassirian P, Kerber N, Heinze D, Zázvorka J, Büttner F, Caretta L, Mann M, Weigand M, Finizio S, Raabe J, Im M Y, Stoll H, Schütz G, Dup B, Kläui M and Beach G S D 2018 *Adv Mater* **30** 1805461
[64] López González D, Shirahata Y, Van de Wiele B, Franke K J A, Casiraghi A, Taniyama T and van Dijken S 2017 *AIP Advances* **7** 035119
[65] Liu Y, Lei N, Zhao W, Liu W, Ruotolo A, Braun H B and Zhou Y 2017 *Appl Phys Lett* **111** 022406
[66] Hierro-Rodriguez A, Quirós C, Sorrentino A, Valcárcel R, Estébanez I, Alvarez-Prado L M, Martín J I, Alameda J M, Pereiro E, Vélez M and Ferrer S 2017 *Appl Phys Lett* **110** 262402
[67] Hierro-Rodriguez A 2017 *Phys. Rev. B* **95** 014430
[68] Ma F, Zhou Y, Braun H B and Lew W S 2015 *Nano Lett.* **15** 4029–4036
[69] Wagner K, Kákay A, Schultheiss K, Henschke A, Sebastian T and Schultheiss H 2016 *Nature Nanotechnology* **11** 432–436
[70] Xing X and Zhou Y 2016 *NPG Asia Materials* **8** e246–8
[71] Albisetti E, Petti D, Sala G, Silvani R, Tacchi S, Finizio S, Wintz S, Caló A, Zheng X, Raabe J,

Riedo E and Bertacco R 2018 *Communications Physics* **1** 1–8
[72] Chang L J, Liu Y F, Kao M Y, Tsai L Z, Liang J Z and Lee S F 2018 *Sci. Rep.* **8** 3910
[73] Hämäläinen S J, Madami M, Qin H, Gubbiotti G and van Dijken S 2018 *Nat. Commun.* **9** 4853
[74] Liu C, Wu S, Zhang J, Chen J, Ding J, Ma J, Zhang Y, Sun Y, Tu S, Wang H, Liu P, Li C, Jiang Y, Gao P, Yu D, Xiao J, Duine R, Wu M, Nan C W, Zhang J and Yu H 2019 *Nature Nanotechnology* **14** 691–697
[75] Banerjee C, Gruszecki P, Klos J W, Hellwig O, Krawczyk M and Barman A 2017 *Phys. Rev. B* **96** 024421
[76] Prosen R J, Holmen J O and Gran B E 1961 *J Appl Phys* **32** S91–S92
[77] Fujiwara H, Sugita Y and Saito N 1964 *Appl Phys Lett* **4** 199–200
[78] Barturen M, Sacchi M, Eddrieff M, Milano J, Bustingorry S, Popescu H, Jaouen N, Sirotti F and Marangolo M 2013 *Eur. Phys. J. B* **86** 478
[79] Soh W T, Phuoc N N, Tan C Y and Ong C K 2013 *J. Appl. Phys.* **114** 053908
[80] Wei J, Zhu Z, Feng H, Du J, Liu Q and Wang J 2015 *J. Phys. D: Appl. Phys.* **48** 465001
[81] Zhou C, Jiang C and Zhao Z 2015 *J. Phys. D: Appl. Phys.* **48** 265001
[82] Jack K H 1951 *Proc. R. Soc. Lond.* **208** 216
[83] Ziegler J F, Biersac J P and Littmark U 1985 *The Stopping and Range of Ions in Solids* (Oxford: Pergamon)
[84] Alameda J M, Contreras M C, Torres M and González Arche A 1986 *J. Magn. Magn. Mater.* **62** 215–220
[85] Ji N, Osofsky M S, Lauter V, Allard L F, Li X, Jensen K L, Ambaye H, Lara-Curzio E and Wang J P 2011 *Phys. Rev. B* **84** 245310
[86] Takahashi H, Igarahashi M, Kaneko A, Miyajima H and Sugita Y 1999 *IEEE Trans. Mag.* **35** 2982
[87] Amarouche T, Garnier L-C, Marangolo M, Eddrief M, Etgens V H, Fortuna F, Sadaoui Y, Tamine M, Cantin J L and von Bardeleben H J 2017 *J. Appl. Phys.* **121** 243903
[88] Bručas R, Hafermann H, Katsnelson M I, Soroka I L, Erikssom O and Hjörvarsson B 2004 *Phys. Rev. B* **69** 064411
[89] Wang G, Dong C, Wang W, Wang Z, Chai G, Jiang C and Xue D 2012 *J. Appl. Phys.* **112** 093907
[90] Cao D, Pan L, Cheng X, Wang Z, Feng H, Zhu Z, Xu J, Li Q, Li S, Wang J and Liu Q 2018 *J. Phys. D: Appl. Phys.* **51** 025001
[91] Corciovei A and Adam G 1971 *J. de Physique Colloque* **32** C1–408–C1–409
[92] Tacchi S, Silvani R, Carlotti G, Marangolo M, Eddrief M, Rettori A and Pini M G 2019 *Phys. Rev. B* **100** 104406
[93] Zhou C, Jiang C and Zhao Z 2015 *J. Phys. D: Appl. Phys.* **48** 265001
[94] Di Pietro Martínez M, Milano J, Eddrief M, Marangolo M and Bustingorry S 2016 *J. Phys.: Condens. Matter* **28** 136001
[95] *en.wikipedia.org/wiki/Triangle wave*
[96] Kittel C 1946 *Phys. Rev.* **70** 965